Modeling of solidification microstructure evolution in laser powder bed fusion fabricated 316L stainless steel using combined computational fluid dynamics and cellular automata

Yi Zhang[1,2], Jing Zhang[1]*

Department of Mechanical and Energy Engineering

[1]Indiana University-Purdue University Indianapolis, Indianapolis, IN 46202

[2]ANSYS, Inc., Evanston, IL 60201

*Corresponding author: jz29@iupui.edu

Abstract

This work presents a novel modeling framework combining computational fluid dynamics (CFD) and cellular automata (CA), to predict the solidification microstructure evolution of laser powder bed fusion (PBF) fabricated 316L stainless steel. A CA model is developed which is based on the modified decentered square method to improve computational efficiency. Using this framework, the fluid dynamics of the melt pool flow in the laser melting process is found to be mainly driven by the competing Marangoni force and the recoil pressure on the liquid metal surface. Evaporation occurs at the front end of the laser spot. The initial high temperature occurs in the center of the laser spot. However, due to Marangoni force, which drives high-temperature liquid flowing to low-temperature region, the highest temperature region shifts to the front side of the laser spot where evaporation occurs. Additionally, the recoil pressure pushes the liquid metal downward to form a depression zone. The simulated melt pool depths are compared well with the experimental data. Additionally, the simulated solidification microstructure using the CA model is in a good agreement with the experimental observation. The simulations show that

---

This is the author's manuscript of the article published in final edited form as:

Zhang, Y., & Zhang, J. (2019). Modeling of solidification microstructure evolution in laser powder bed fusion fabricated 316L stainless steel using combined computational fluid dynamics and cellular automata. Additive Manufacturing, 28, 750–765. https://doi.org/10.1016/j.addma.2019.06.024

higher scan speeds result in smaller melt pool depth, and lack-of-fusion pores can be formed. Higher laser scan speed also leads to finer grain size, larger laser-grain angle, and higher columnar grain contents, which are consistent with experimental observations. This model can be potentially used as a tool to optimize the metal powder bed fusion process, through generating desired microstructure and resultant material properties.

Keywords: laser powder bed fusion; stainless steel; microstructure; cellular automata; computational fluid dynamics

1. Introduction

In recent years additive manufacturing (AM) shows considerable progress in fabricating complex shaped parts for industrial applications[1]. One of the biggest challenges for laser powder bed AM is to control the microstructure and the properties of the as-built parts. The processing parameters, such as laser power, scan speed, can affect the microstructure of the fused part, which will influence the mechanical properties of the AM product. Efforts have been made to better understand the correlations of processing parameters and the microstructures of the product by means of experimental[2, 3] and computational studies [4-7]. The laser powder bed fusion process involves phenomena such as optical absorption, heat conduction, convection, radiation, metal phase change, surface tension-driven fluid flow, recoil pressure [4, 8-11]. These complicated phenomena demand the need for developing a comprehensive modeling framework for the laser powder bed fusion process.

At mesoscale, the main phenomena during the laser powder bed fusion process can be modeled as a laser heat-driven fluid flow problem. For this reason, computational fluid dynamics (CFD) becomes a suitable tool for the modeling of this process. Different from the traditional welding models, the geometrical irregularity of the sintered powder often causes more complicated temperature distribution and unstable fluid flow [12-14]. The powder melting process, as well as the driving forces for fluid flow, have been studied by numerous papers [5, 10, 14-16]. Microscopic defects due to lack of fusion at low energy density, and keyhole pores at higher energy density, have been reported [17]. In the CFD based models, the construction of the laser model is critical. For the conventional welding simulations that involve melt pool flow, the laser power is usually represented by a volumetric heat source since it can take into account the effect of laser penetration in metals[18]. For a volumetric heat source, an energy density (unit: J/m^3) is

applied to a selected volume with the distribution that varies along the depth. The distribution function is established based on the cases of laser-flat surface interaction. However, for the powder bed fusion process, where the powder bed surface is not flat, the validity of this method is limited. In the powder bed fusion process, heat is generated where the laser beam strikes the particle surface, and then the heat is diffused into the particle. Also, the shadowing effect, where some bottom particle surfaces could be prevented from heating by shadows of other particles, is a unique feature in the PBF process[19]. Laser rays may be absorbed by the top surface of the particle and they cannot penetrate to the bottom surface of the particle, which could lead to lack-of-fusion pores – a unique phenomenon in powder bed fusion process. When lack-of-fusion pores exist, the particle bottom will have a smaller contact region with the previous layer which decreases the heat dissipation, so that more heat is accumulated inside the particle, so that particle could be partially melted. For the volumetric heat source, melting occurs at anywhere inside the particle simultaneously. Neither partial melting of particles, nor the shadowing effect could be captured. Khairallah *et al.*[19] developed a "simplified ray-tracing" laser model, which assumes the laser as a surface heat source (J/mm^2) that generates heat when the laser rays hit on powder surface for the first time. Although only the first laser-metal interaction is modeled without considering the reflection, unique phenomena in powder bed fusion, such as partial particle melting, shadowing, and spattering can be simulated with this laser model. Although some of the above-mentioned CFD studies provide information on the microstructure of the fused powder[20], only qualitative analyses are provided without microscale grain structure. The Cellular Automaton (CA) has become an appropriate tool for the prediction of microstructures during the metal solidification process. The application of CA on modeling of solidification was first introduced by Gandin and Rappaz [21]. After that, the method and the

coupling techniques to finite element were further improved by the same group [4, 22]. Based on that, methods including phase field modeling (PFM)[23], cellular automata (CA)[24, 25], and coupled cellular automata finite element (CAFE)[26], have been developed and applied for predicting grain solidification and dendrite growth during metal molding process. Prediction of grain structure during the laser or arc welding process was studied recently [11, 27-30]. In Chen's work [29], the air-metal two-phase CA modeling approach was applied, which enables the CA to simulate the welded metal free surface. Direct application on additive manufacturing process is recently reported [31-33], but a three-dimensional (3D) CA model with a realistic powder bed configuration is still absent.

Due to the complex geometrical evolution of the powder bed during L-PBF process, a combined modeling framework that incorporates CFD metal surface tracking and grain structure prediction is imperative. Recently, a multiscale modeling approach that combines CFD and CAFE (cellular automata finite element) method for selective laser sintering has been reported by Panwisawas *et al.* [34]. Temperature history from CFD simulation was used for CA modeling. However, the metal surface configuration during the scanning was not considered in the CA microstructure prediction. Instead, only the final configuration from the CFD result was used. This assumption will lead to inaccurate results when the powder bed layer thickness is large, where the metal surface changes rapidly during the laser scanning process. Moreover, although there are computational studies on the laser scan speed effect on the powder bed fusion process[10, 20], most of them are at the macro or meso scale. The associated microstructure and grain morphology are rarely reported. Recently, a framework using CA+CFD method was proposed to predict microstructure and/or even material properties [35, 36]. It is noted that these studies are focused on developing the framework or the concept of combined models, experimental

comparison or application to AM process design is lacking. Our work presents a detailed study of the effect of AM processing parameters on microstructures, and experiment validation and comparison are presented.

In this work, a novel multiscale modeling framework is developed. This model starts with a randomly packed powder bed with predefined size distribution, as the initial powder bed structure. It uses the CFD based powder melting model with the "simplified ray-tracing" heat source (Khairallah *et al.*[19]) to predict the temperature and free surface morphology, and it uses air-metal two-phase based CA method to predict the microstructure of the powder bed fused metal material. With the modeling framework, the scan speed effects on microstructure and grain shape, size, orientations are studied in detail.

2. Method

Laser powder bed fusion process is a complex process. To simulate this process, multiple physical phenomena need to be taken care of. Therefore, in this work, a multiscale simulation framework is developed. This framework includes:1) a discrete element model (DEM) to generate the initial powder bed packing configuration, 2) a CFD model to simulate the laser-powder interaction, and to predict the temperature and free surface configuration and 3) a CA model to simulate the solidification process and to predict the solidification microstructure evolution of the laser powder bed fusion process.

2.1. DEM powder deposition

The meso scale laser powder bed uses the initial powder configuration from a discrete element model (DEM) based powder deposition process. Particles are simulated through solving

Newton's second law of motion and rigid body dynamics equation combined with specific time-stepping algorithms in LIGGGHTS package[37]. The equations of motion for the particle translation and rotation are defined by Newton's second law[38]:

$$m_i \ddot{\boldsymbol{x}}_{\boldsymbol{i}} = m_i \boldsymbol{g} + \sum_j \boldsymbol{F}_{\boldsymbol{ij}} \quad (1)$$

$$I_i \ddot{\boldsymbol{\theta}} = \sum_i (\boldsymbol{r}_{\boldsymbol{ij}} \times \boldsymbol{F}_{\boldsymbol{ij}}) \quad (2)$$

where m_i is the mass of particle i, $\ddot{x}_i$ is the translational acceleration of particle i, g is the gravity constant, and F_{ij} is the force acting on particle i, given by particle j. For the rotational motion, I_i is the moment of inertia of particle i, $\ddot{\theta}$ is the angular acceleration of particle i, $\sum_i (r_{ij} \cdot F_{ij})$ represents the total rotational force acting on particle i from the rest of the system.

The interaction of particles is calculated based on Hertzian contact force[39, 40]:

$$F_{\mathrm{hz}} = \sqrt{\delta}\sqrt{\frac{R_i R_i}{R_i + R_j}}\left[\left(k_n \delta n_{ij} - m_{eff}\gamma_n v_n\right) - \left(k_t \Delta s_t + m_{eff}\gamma_t v_t\right)\right] \quad (3)$$

with R_i and R_j as the radii of particle *i* and *j*, respectively, δ the overlap distance of two particles, *k* the elastic constant, γ the viscoelastic damping constant, n_{ij} the unit vector along the line connecting the centers of the two particles, *v* the component of the relative velocity of the two particles; indices *n* and *t* referring to normal and tangential contact respectively. F_{hz} is the force calculated using the Hertzian equation, and m_{eff} is the effective mass of two particles.

To generate the powder bed configurations using the DEM, a box with rigid walls is placed at the bottom of the model, and the particles are inserted from the top of the box. Then, the particles freely drop down to the box by gravity. The particle size follows a normal distribution with a mean radius of 27 μm and a standard deviation of 2.1 μm. A powder layer with a thickness of 80 μm is generated by the DEM and the location and radius of each particle are passed to the next step CFD model as the initial condition. The powder configurations, including powder size, distribution, and layer thickness are chosen according to Yadroitsev *et al*.[41]. It allows

comparing the modeling results in this work with the experimental data in the literature. In the actual L-PBF process, a recoating rack is applied to control the powder layer thickness. However, the recoating process is not simulated in this work. In the DEM model in this work, excessive particles are deposited in the simulation box to ensure the thickness is greater than the desired thickness (80 μm). And then, any particles that have the top surface height (center height + radius) greater than 80 μm are removed from the DEM result. By doing this, the recoating rack and powder bed interaction are mimicked, and the desired layer thickness is obtained. The final packing density in the DEM result is ~51%, which is in a reasonable range observed in experimental measurements in the literature (50% -61%) [42, 43]. The particle trajectories during the DEM powder deposition simulation and the resulting powder layer configuration are shown in Figure 1 (a) and (b), respectively.

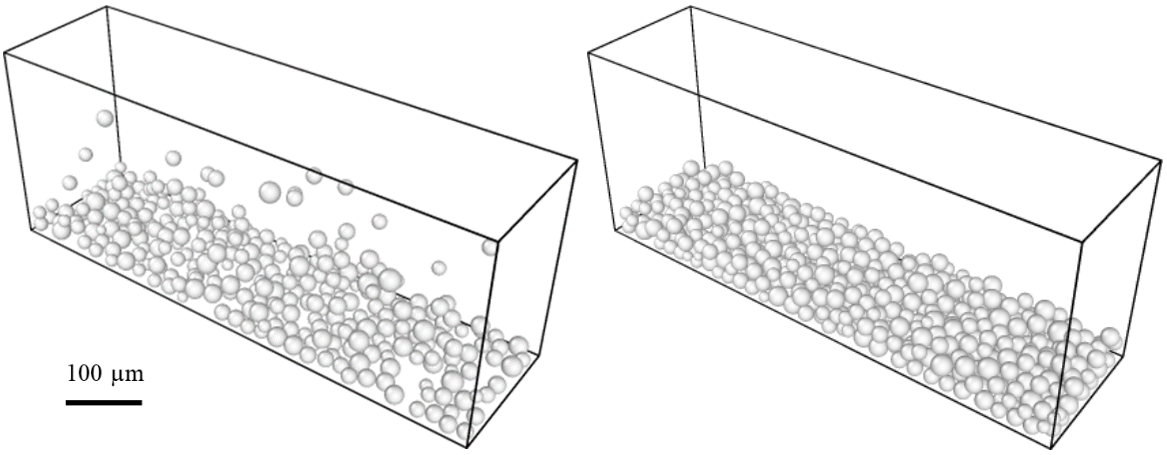

(a) (b)

Figure 1: (a) DEM simulated powder trajectory during the powder deposition, and (b) the powder layer generated by DEM.

2.2. CFD laser-powder bed interaction

The interaction of the laser and powder bed is investigated by developing a thermal-fluid model. In this model, a moving laser heat source is applied to the top surface of the powder bed, and the flow of the molten metal is studied. This model is based on the conservation of mass equation, momentum equation, energy equation and the Volume of Fluid (VOF) equation. Complicated physical phenomena, including melting, buoyancy-driven flow, surface tension, Marangoni convection, and metal evaporation induced recoil pressure, are also included in this work by developing User Defined Functions (UDF) in ANSYS Fluent[44]. The flow in this model is assumed as incompressible Newtonian laminar flow, the need for a turbulent model has not yet been proven [6, 18, 45-48]. The laser source is modeled by applying a surface heat source that consists of vertical rays with a Gaussian energy distribution with "simplified ray-tracing" method proposed by S. A. Khairallah *et al.* [19], which considers only the first laser-metal interaction without reflection. The advantage of this method is that it can produce multiple physical phenomena, like shadowing, comparing to volumetric heat sources. Some more complicated laser models with reflection have been reported, but they are mostly for keyhole dynamics in laser welding and they can spend extreme computational costs, therefore they are not adopted in this study.

Assuming both molten metal and air phases in the model are incompressible fluids, the mass conservation equation gives:

$$\frac{\partial \rho}{\partial t} + \boldsymbol{\nabla} \cdot (\rho \boldsymbol{u}) = 0 \tag{4}$$

where ρ is the density, t is time, $\boldsymbol{u}$ is the flow velocity. The simulation domain is composed of two phases: the metal phase φ_1, includes both liquid and solid metal; and the air phase φ_2. The term φ is volume fraction, it ranges from 0 to 1, and for any location in the domain, the

summation of two phase volume fractions is unity[49], the volume fraction conservation equation is[50]:

$$\varphi_1 + \varphi_2 = 1 \tag{5}$$

$$\frac{\partial \varphi}{\partial t} + \boldsymbol{\nabla} \cdot (\varphi \boldsymbol{u}) = 0 \tag{6}$$

Therefore, the metal free surface is the iso-surface where the volume fraction $\varphi = 0.5$, and its updating with time. To solve the velocity field, the Navier-Stokes equation is applied[18]:

$$\frac{\partial}{\partial t}(\rho \boldsymbol{u}) + \boldsymbol{\nabla} \cdot (\rho \boldsymbol{u} \times \boldsymbol{u}) = -\boldsymbol{\nabla} p + \boldsymbol{\nabla} \cdot \{\mu[(\boldsymbol{\nabla u} + \boldsymbol{\nabla u}^T)]\} + \rho \boldsymbol{g}[1 - \beta(T - T_m)] + K(T)\boldsymbol{u} + \boldsymbol{F_s} \tag{7}$$

where p is the static pressure, μ is the viscosity, g is the gravitational body force, $\rho \boldsymbol{g}[1 - \beta(T - T_m)]$ is the buoyancy force term induced by the temperature dependency of density, $K(T) = \frac{(1-f_l)^2}{({f_l}^3+\epsilon)} A_{mesh}$ is a Darcy condition that suppress the motion of un-melted metal, where f_l is the liquid fraction, $\epsilon = 0.01$ is a small number to avoid zero denominators, and $A_{mesh} = 10^{14}$ is the mesh zone constant. $\boldsymbol{F_s}$ is the additional momentum source term, and in this work, the source term that applied at the metal-air interface is [18, 19]:

$$\boldsymbol{F}_s = (\sigma \kappa \hat{\boldsymbol{n}} + \boldsymbol{\nabla}_t \sigma + P_v \hat{\boldsymbol{n}}) \left| \vec{\nabla} \varphi_1 \right| \frac{2\bar{\rho}}{(\rho_1 + \rho_2)} \tag{8}$$

$$P_v = 0.54 P_a e^{\left(\frac{\lambda}{K_B}\left(\frac{1}{T} - \frac{1}{T_b}\right)\right)} \tag{9}$$

$$\bar{\rho} = \varphi_2 \rho_2 + (1 - \alpha_2)\rho_1 \tag{10}$$

where σ is the surface tension, κ is the interface curvature, $\hat{n}$ is the surface normal, ∇_t is the tangential gradient, $\left|\vec{\nabla}\varphi_1\right|$ is the interface delta function, and the average density $\frac{2\bar{\rho}}{(\rho_1+\rho_2)}$ at the interface is to smear out the density sudden jump between the hard phase and the soft phase. The surface temperature below the laser spot can easily reach the metal's boiling point, which causes ejection of vapor gas. For each evaporation location, the vapor gas ejects normal to the molten

metal free surface at that specific location, and the overall vapor gas flow is the summation of all the evaporation locations. The overall vapor gas flow direction depends on the shape of the melt pool cross section, so that the direction of the overall vapor gas flow changes with varying laser scan speed[12, 14]. The vapor recoil pressure adds forces to the surface of the molten metal that generates a surface depression below the laser spot. The direction of the recoil pressure is opposite to the vapor gas direction and point into the molten metal surface due to momentum balance. There are some phenomenological models that can correlate the temperature to recoil pressure magnitude [9]. In this work, the simplified model developed by Anisimov [8] is employed as suggested by Khairallah *et al.* [19] in their recent L-PBF modeling work. As shown in Equation (9), the recoil pressure magnitude is an exponential function of T. P_a is the ambient pressure of 1 bar, λ is the evaporation energy, K_B is the Boltzmann constant, and T_b is the boiling temperature.

The heat transfer is simulated by solving temperature T in the energy equation in fluids. For the time-dependent energy equation in fluid [11, 34, 47, 51]:

$$\frac{\partial \rho C_p T}{\partial t} + \boldsymbol{\nabla}\left(\rho \boldsymbol{u} C_{\boldsymbol{p}} T\right) = \boldsymbol{\nabla} \cdot \mathrm{k} \boldsymbol{\nabla} T - Q \tag{11}$$

where the term $\nabla\left(\rho \boldsymbol{u} C_{\boldsymbol{p}} T\right)$ is convection within the fluid due to fluid flow and Q is the energy loss due to various reasons, including convection, radiation, fluid melt and evaporation, and laser heat sources. Expanding the heat loss term Q by plugging in Newton's convection equation, radiation equation, the melting/evaporation heat loss, and the laser heat source, the energy equation becomes [18]:

$$\frac{\partial \rho C_p T}{\partial t} + \boldsymbol{\nabla}\left(\rho \boldsymbol{u} C_{\boldsymbol{p}} T\right) = -\frac{\partial \rho \Delta H_f}{\partial t} - \nabla\left(\rho u \Delta H_f\right) + \boldsymbol{\nabla} \cdot \mathrm{k} \boldsymbol{\nabla} T - \left\{\left[h_c\left(T - T_{ref}\right) + \sigma_s \varepsilon\left(T^4 - T_{ref}^4\right) + Q_v\right] - S_{laser}\right\} \left|\vec{\nabla} \varphi_1\right| \frac{2\overline{C_p}\,\overline{\rho}}{\left(C_{p1}\rho_1 + C_{p2}\rho_2\right)} \tag{12}$$

where C_p is the specific heat, k is the thermal conductivity, h_c is the convection coefficient, at the metal-air interface, T_{ref} is the reference temperature, σ_s is the Stephan's constant and ε is the

emissivity, ΔH_f is the fusion enthalpy change. $Q_v = \Delta H_v J_v$ is the evaporation heat loss caused by the evaporation mass flux, $J_v = {0.82P_v}/{\sqrt{2\pi MRT}}$, where M is molecular mass and R is the gas constant. Note that all the heat loss terms are imposed on the metal-air interface of the fluid domain, therefore the interface delta $|\vec{\nabla}\varphi_1|$ is multiplied at the end. Similar to Equation (8), material properties at the interface are averaged by the term $\frac{2\overline{C_p}\overline{\rho}}{(C_{p1}\rho_1+C_{p2}\rho_2)}$ in order to smear out the sudden jump between two phases, therefore enhance the numerical convergence. The Gaussian distributed laser beam intensity (power per unit area) S_{laser} is represented as [10]:

$$S_{laser} = \frac{\alpha P}{\pi {r_0}^2} exp\left\{-\frac{2[(x-v_{laser}t-x_i)^2+(y-y_i)^2]}{{r_0}^2}\right\} \quad (13)$$

where P is the laser power, α is the absorbtance, r_0 is the laser radius at ${1}/{e^2}$, v_{laser} is the scan speed of the laser, x_i, y_i is the initial position of the laser focal center. The ray-tracing of the laser is applied by projecting the laser power to the top surface of the metal, and all the heat source is absorbed by the top surface at the first interaction, which means there is no optical reflection occurs in this model.

Equations 4, 6, 7, 12 are solved in the finite volume implicit integration scheme. Three different laser scan speed are imposed on the same powder initial configuration, the materials for 316L stainless steel, the laser heat source model and the process parameters are tabulated in tables 1-2. The temperature dependent thermal-physical properties are plotted in Figure 2. The initial condition of the metal and air phases are mapped from the DEM powder deposition result (Figure 3). A mesh size of 3μm is applied in order to provide high enough resolution to represent each individual metal particle explicitly. Due to such a small mesh size, the time step of 0.5 μs was applied to ensure convergence by maintaining the Courant number is less than 0.99 throughout the simulation.

Table 1: Thermophysical properties of 316L stainless steel for laser powder bed fusion[19, 52]

Material	316L Stainless Steel
Solidus (K)	1658
Liquidus (K)	1723
Molar mass (kg/mol)	0.055845
Surface tension (Pa)	3.282-0.00089T
Viscosity (Pa s)	5
Latent heat of fusion (kJ/kg)	260
Evaporation enthalpy(J/kg)	415000
Emissivity	0.1(Liquid)/0.4(Solid)
Stefan-Boltzmann constant	5.67E-08
Boiling point (K)	3086
Atmosphere pressure(Pa)	10325
Reference temperature(K)	300

Table 2: Laser heat source model and process parameters in the simulation

Parameter	Value
Laser power (W)	50
Absorption coefficient	0.23
Laser radius (μm)	35
Laser scan speed (m/s)	0.12, 0.20, 0.28

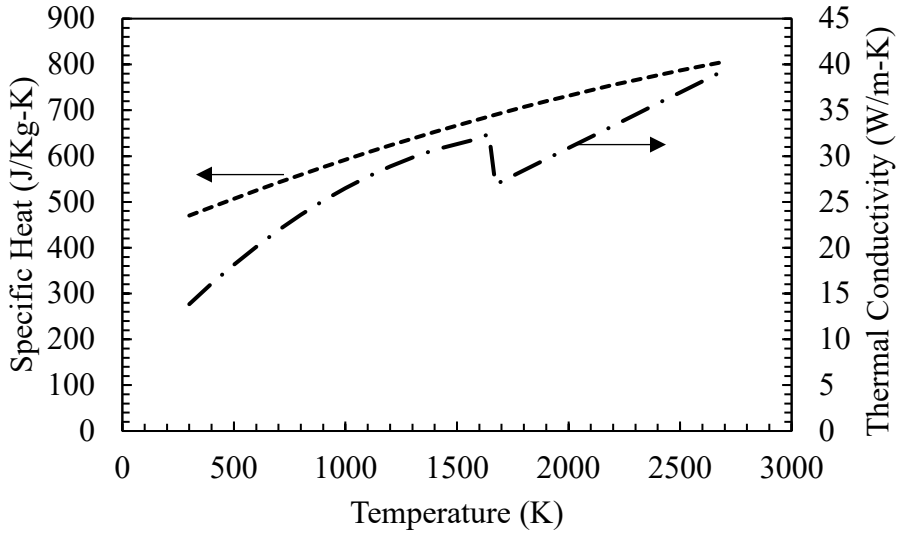

(a)

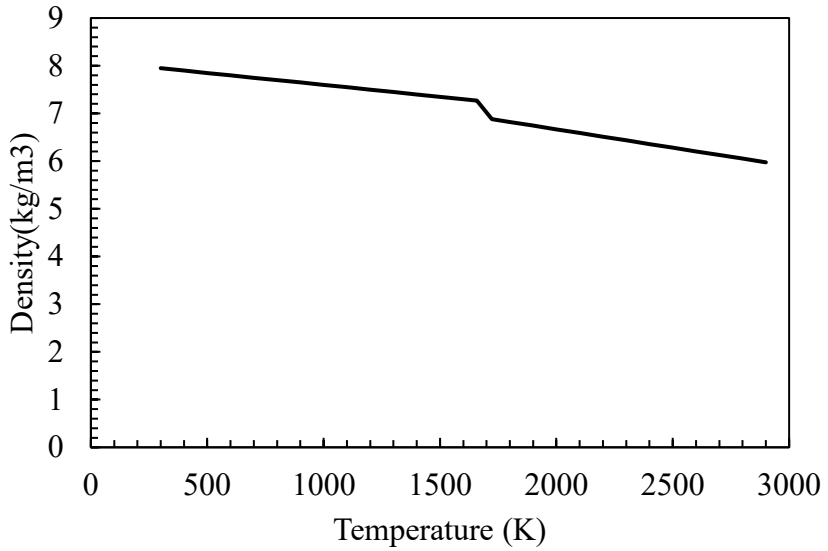

(b)

Figure 2: Temperature dependent (a) specific heat and thermal conductivity, and (b) density used in this model.

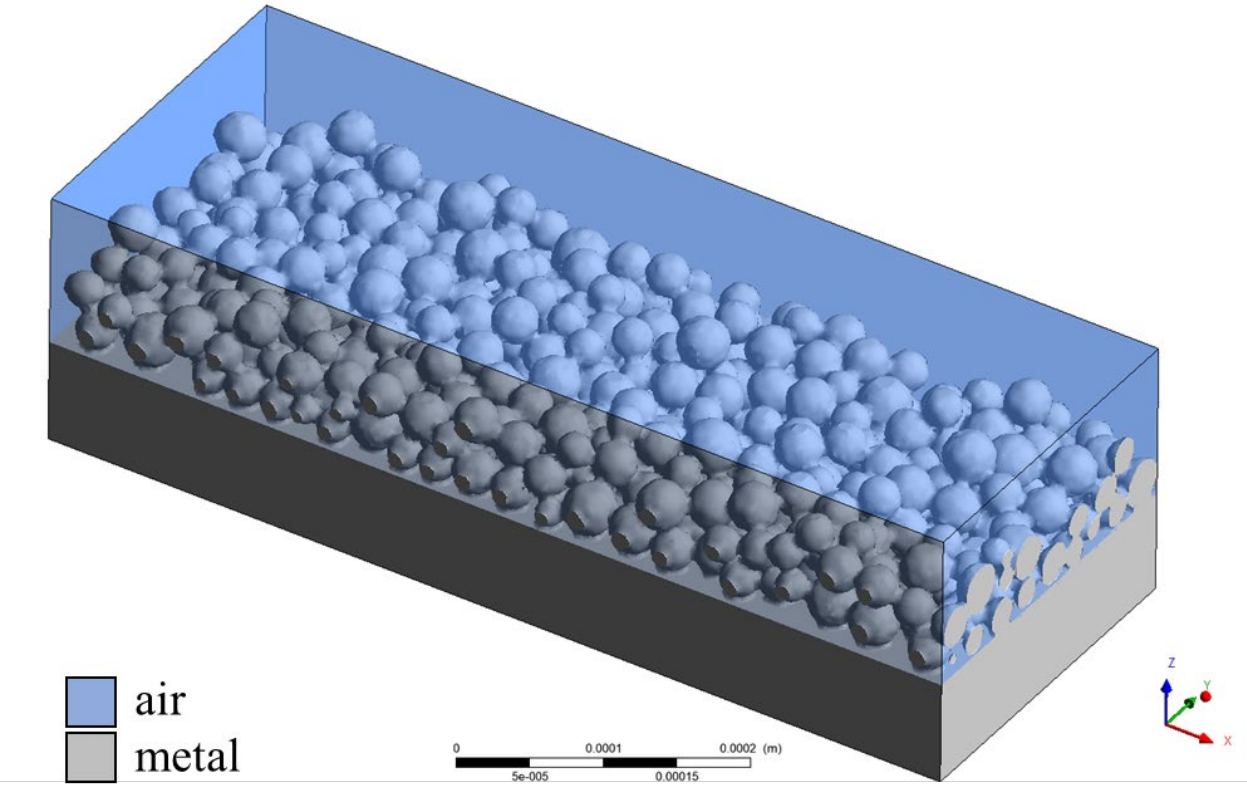

Figure 3: Initial configuration for the CFD simulation mapped from DEM powder deposition result. Colors show the metal (including solid and liquid), and air phases in the two-phase flow model.

2.3. CA solidification

The microstructures of solidified grains are simulated using the CA method. In a typical CA model, the simulation domain is discretized to uniform-sized "cells" with a square shape (in 2D) or a cubic shape (in 3D). Each cell contains one or more variables to represent property or states of the current cell. The state of each cell may change during the simulation, according to some pre-defined cellular automata rules. These rules usually consider the states of the current cell and the states of its neighboring cells. von Neumann neighborhood and Moore neighborhood are the commonly used definitions of cell neighbors. In this work, the Moore neighborhood, which contains 26 nearest neighbors in 3D, is applied. The CA simulation is discretized to time steps, in

each time step, the states of every cell are updated following CA rules. The results from CA simulations are presented by the evolution of the states of cells.

During the solidification process of metals, some nuclei will form at the fusion line and the melt pool volume, and then they will expand to form larger grains. For each of the nucleus, its surrounding material will solidify by forming crystals next to the nucleus with the same crystal orientation. Therefore, the growth of each grain will follow some specific directions, which is the crystallographic orientation of its nucleus. For 316L stainless steel, most of the crystals are face-centered cubic (FCC), so that the ideal shape of the grain will be an octahedron. All the grains expand along the three diagonal directions of the octahedral, and the growth rate of each dendrite tip depends on its local temperature (see Figure 4 for an example). The diagonal directions of the octahedron are the x,y,z, axis of the local coordinates of each grain, and the Euler angles (α,β,χ) between local and global coordinate axis are the grain orientation angles.

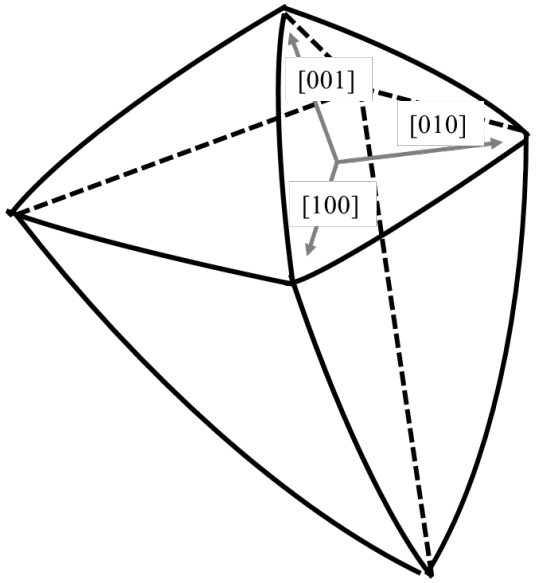

(a)

Figure 4: The shape of a grain grown in a non-uniform temperature condition. The arm lengths are different due to different local temperature at the dendrite tips.

For the simulation of solidification, each cell contains two variables: 1) The orientation variable "O" that represents the grain orientation of each cell, and 2) The cell state variable "I", which indicates if the cell is liquid/mushy/solid. In the program, instead of storing the actual Euler angles to each cell, the orientation of solid metal cells is represented by integer classes of 1-48, which linearly scales the Euler angles ranging from -45°~45°. The purpose of reducing the Euler angles to integer class is to reduce the read/write effort during the computation, since integer operations are faster than double/float number formats, and Euler angles could be float/double numbers in the program. Integers only need to be projected back when Euler angle based evaluation is required (octahedra vertices evaluation, for example). As suggested by Rappaz et al[53], 48 classes are enough to represent the microstructure and reduce the complexity of the program. On the other hand, the orientation of liquid metal cells is set to zero (O = 0). In addition, the CA simulation domain contains both metal and air phases, and only the metal will undergo the melting/solidification process. Therefore, the orientation of the air phase is a negative integer (O = -10). The initial structure of the powder (SS grade 316L, Sandvik Osprey Ltd.) was consists of equiaxed grains with the grain size of 1~2.5μm, and the initial grain size of the 316L substrate was unknown[54]. Therefore, in the CA model, a randomly orientated grain structure is generated by assigning a random number (follow a uniform distribution function) to each cell in the CA domain, representing a 1μm initial grain size of the powder and the substrate.

The one-way coupling between the CFD and the CA models is illustrated in Figure 5. Temperature and metal/air distribution in the domain at each CFD time step are imported to CA as inputs. The CA simulation domain is smaller than the CFD, since a much finer mesh is required for the CA model. The CA cell size should be small enough to illustrate the grain

structures with the grain size of 5-30 µm. In the CFD model, the domain size is $720 \times 270 \times 210\ \mu m^3$ with a mesh size of 3 µm, whereas in the CA model, $441 \times 139 \times 123\ \mu m^3$ domain is simulated with a cell size of 1 µm. The temperature (T) and metal distribution (VOF) are linearly interpolated in "x,y,z" from the CFD domain to the CA domain. Similarly, the required stable time steps for the CFD (0.5 µs) and the CA (0.2 µs) models are different, so that the CA inputs at different time steps are from linearly interpolated CFD results based on time "t". In Figure 5, the air phase (O = -10) is not shown for the illustration of the initial powder configurations.

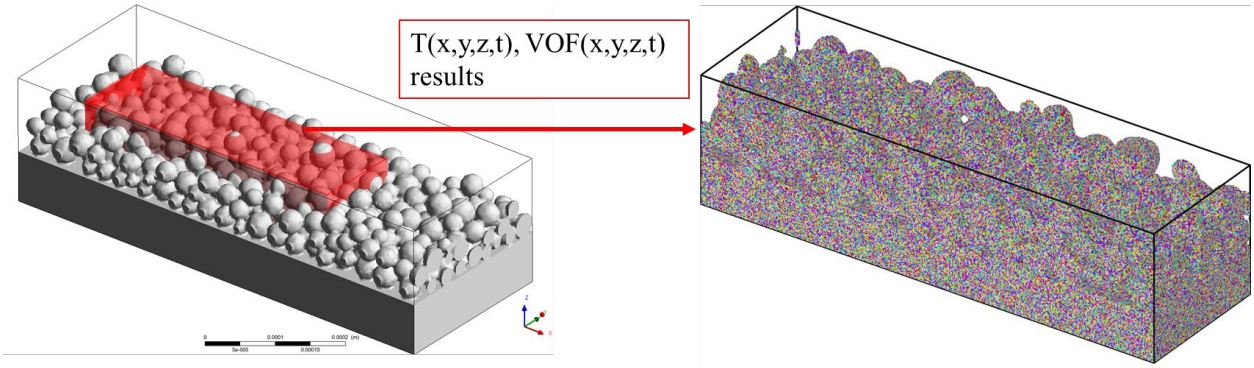

Figure 5: Simulation domains of CFD (left) and CA (right) models. The red block region in the CFD model shows the CA domain.

In the CA model, two physical processes, melting and solidification, are simulated within each of the time step. Figure 6 shows the workflow of the CA method. There are two processes, melting and solidification, within each time step. In the melting process, the temperature and volume of fraction results are passed from the CFD model. At a specific time step, if a cell has temperature larger than liquidus T_L of the material, then its orientation will be reset to zero, meaning the cell is liquid and it is subject to the solidification simulation. The volume fraction is updated to track the free surface of the metal. There are two possible nucleation mechanisms in the solidification process. The formation of nuclei at the fusion line is called boundary nucleation, and the

formation of nuclei that are not adjacent to the fusion line is called volume (or bulk) nucleation. Boundary nucleation occurs before volume nucleation, since it requires less undercooling, therefore, with different processing conditions, the actual nucleation could be either boundary nucleation only, or a mixture of boundary and volume nucleation. To represent the volume nucleation formed equiaxed grains in the simulation model, an undercooling-nucleation density function is necessary as an input. However, this data is currently not available for the specific material in this study, so that the volume nucleation is ignored. The current CA model only considers nucleation from the fusion boundary, where each solid cell at the boundary represents a boundary nucleus for the subsequent grain growth simulation.

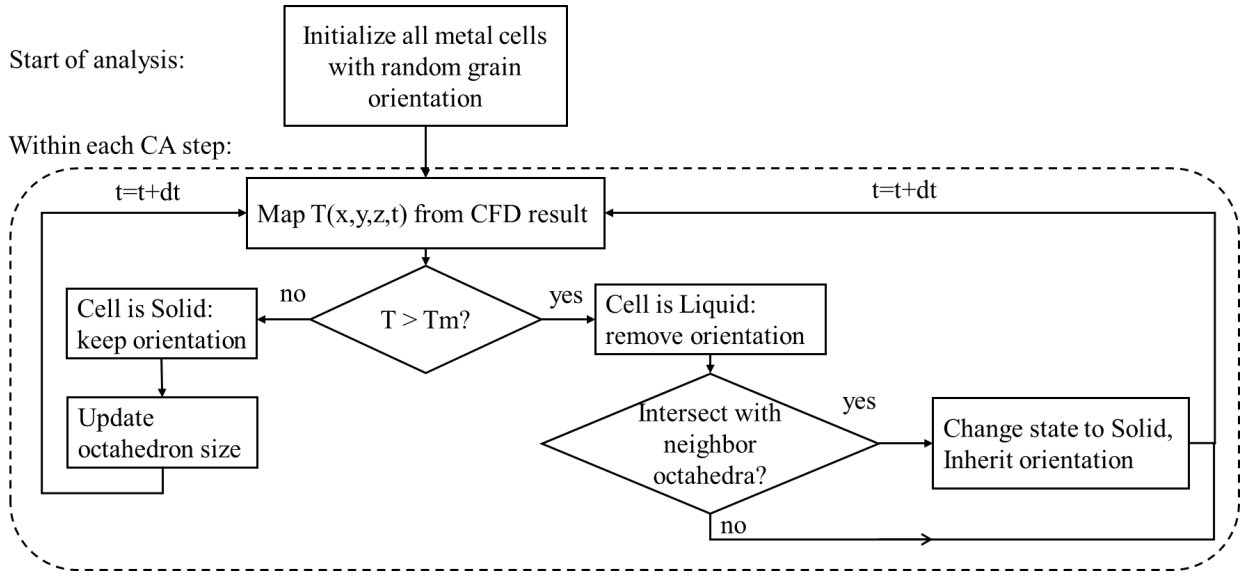

Figure 6: Workflow of the CA method with inputs from CFD results.

The solidification of material is indeed the transformation of liquid state to solid-state around the liquid-solid interface, so it is necessary to update the cell states. For the cell state variable, there are four possible values, the “liquid not at the interface” (I = 0), which represents a liquid cell that not located at the solid-liquid interface; “liquid at the interface” (I=1), indicating a liquid cell

at the solid-liquid interface. Similarly, the solid cells are divided to “solid at the interface” (I = 2) and “solid not at the interface” (I = 3). In each time step, after the cell orientations are updated by the melting process, the cell state variables are calculated based on the orientation, “O”, of every cell and its neighborhoods.

In the solidification process, the transformation from liquid at the interface to solid at the interface (I = 1 > I = 2) is modeled using the “modified decentered square” method[23]. The schematic of this method is shown in Figure 7. The problem is simplified to 2D for better illustration. In this method, an interface solid cell “i" ($I_i = 2$) has a growing “square” with respect to the grain orientation (θ). The diagonal length “L” (half diameter of the dashed square in Figure 7(b)) will increase within time increment Δt by the following equation:

$$L_i = \sum_t V_i \Delta t \qquad \text{if } I_i = 2 \tag{14}$$

where V_i is the growth rate of the grain, which is a function of temperature T[5]:

$$V_i = A\Delta T_i^{\,2} \tag{15}$$

$$\Delta T_i = T_{liquidus} - T_i \tag{16}$$

Here the material specific constant “A” can be obtained by either analytical equations [55] or phase field models [11]. In this work, the value of $A = 2 \times 10^{-7} m/(K^2 s)$ [56] is applied.

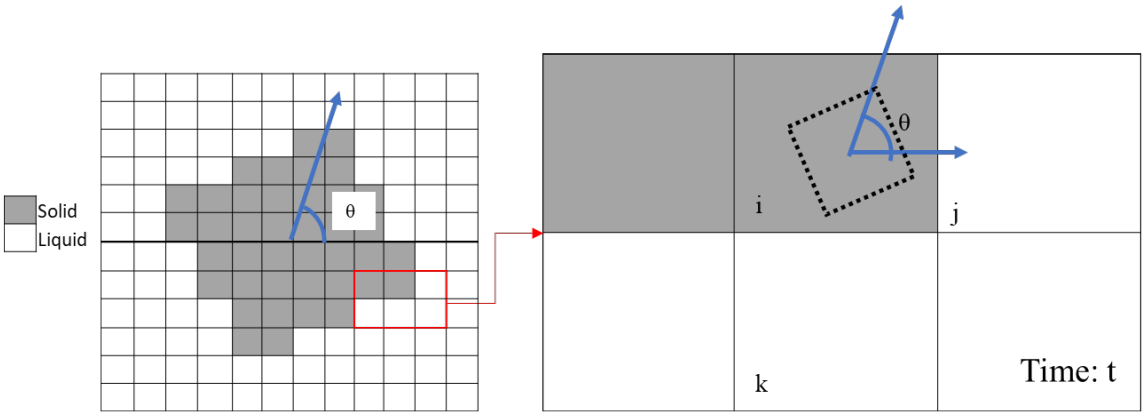

(a) (b)

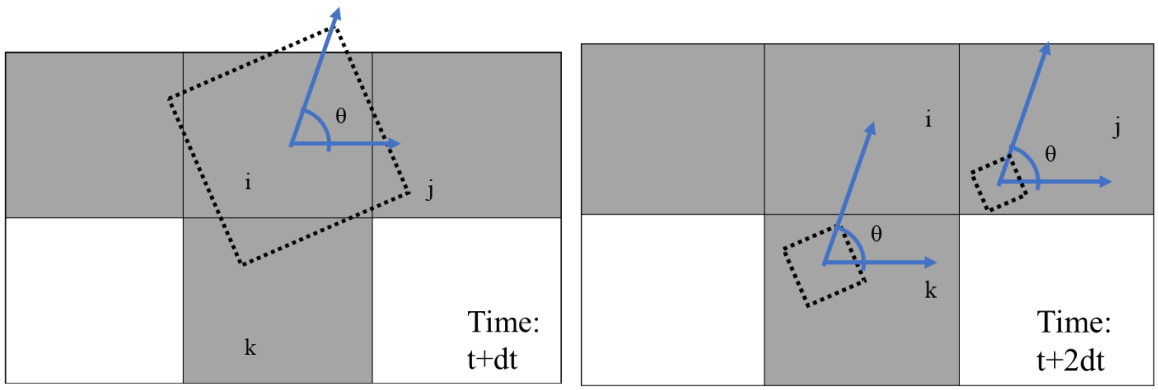

(c) (d)

Figure 7: Schematic of the modified decentered square method for solidification.

At an instant when the square is large enough to intersect with any of the neighboring cells of "i" (Figure 7(c)), the states of cells "j" and "k" turn to "solid at the interface" (I = 2), indicating that these cells have been solidified by cell "i". At the same time, cells "j" and "k" will inherit the orientation of cell "i" ($O_j, O_k = O_i$), indicating they will be the same grain with identical orientation. In the next time step (Figure 7(d)), since the states of cells "j" and "k" are "solid at the interface", they will start growing their own squares with calculated L_j, L_k, as the two black dash squares in Figure 7(d), but the centers of these newly generated squares are the intersecting vertex from cell "i", which is not necessarily to be the center of the cell.

In 3D models, the "squares" turns out to be "octahedra", and the Euler angle has three components, instead of the "θ" in 2D case. Not that in Equation 13, the length increment $V_i \Delta t$ within each time step should never exceed the cell side length. Otherwise, the growth algorithm will not valid anymore. A constant time step of 0.2 μs is used for the CA simulation to avoid erroneous results. Variable time step based on maximum V_i would be ideal in order to improve

the efficiency, but it is not applied in this work. To achieve a better understanding, the cell state transition rules are summarized in Table 3.

Table 3: Cell state transition rules in the CA model. T is the local temperature of a cell, T_L is the liquidus.

Process	cell state before transition	Transition test	State after transition
Melting	2,3	$T > T_L$ AND all neighbors are liquid (I<=1)	0
	2,3	$T > T_L$ AND solid (I>=2) cell exist in neighbors	1
Solidification	0	At least one solid (I>=2) cell exists in neighbor cells	1
	1	Intersected with "decentered-square"	2
	2	All neighbor cells are solid (I>=2)	3

In this work, the CFD model was developed in the commercial simulation package ANSYS Fluent 17.0. In addition to the features that Fluent already have, the source terms in both energy and momentum equations were added to the model by using User Defined Functions (UDF). The energy source terms include laser heating and interface heat convection/radiation, and the momentum source terms include recoil pressure. With two 12-core Intel Xeon E5-2680 v3 CPUs with 24 processors, the CFD model ran for 20 hours in average.

The CA modeling algorithm was coded in MATLAB[57], and the visualization of CA results was done by Ovito[58]. For the solidification analysis in this work, the total computation time was about 17 hours on one processor of an Intel Xeon E3-1505 CPU. So far, this program is only capable of serial computation, the computation cost will be greatly reduced by parallel computations as illustrated by Lian *et al.*[59] and Yan *et al*.[59].

3. Results and discussion

3.1. Model validation

The CFD model generates the temperature distribution history and the metal surface configuration, which are the two critical inputs for the microstructure prediction. Therefore, a validation of the CFD result is needed.

In the validation case, a simulated powder bed configuration is generated. In the CFD model validation, the laser melting of a 316L stainless steel bare plate is simulated and compared with the experiment done by Gusarov [4]. A 316L stainless steel subjected to a single path 0.12 m/s constant speed laser scan is simulated. The laser power is 45 W and the full width at half maximum(FWHM) of the laser beam is 60 μm. The resulting melted region is compared with the experimental work [4]. The comparison of the cross-section along the scan direction is shown in Figure 8. The width and depth of the melted region are compared. As list in Table 4, the differences between modeling and experiment are 5.7% and -4.8%, respectively. The errors are in a reasonable range, given that some of the high-temperature properties in the model are not available and are obtained by theoretical estimations[52].

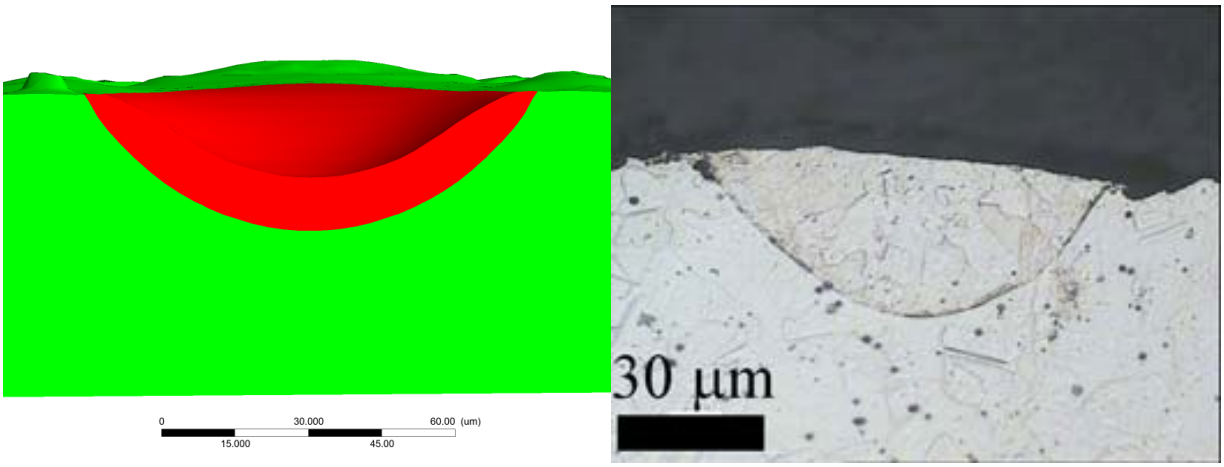

(a) (b)

Figure 8: (a) The simulated melted region cross-section by CFD model. Red shows the melted metal. (b) the optical image from the experiment.

Table 4 Comparison of the simulated melt pool width and depth with experiment[46].

	Width (um)	Depth (um)
Experiment[4]	86.25	32.34
This work	91.21	30.76
Difference	5.7%	-4.8%

3.2. Effect of scan speed on melt pool and microstructures

The single-track laser powder bed fusion processes using the parameters listed in Table 2 are simulated by the multiscale modeling frame that we presented above. Three simulation cases are conducted with laser scan speeds of 0.12 m/s, 0.20 m/s and 0.28 m/s. A $720\mu m \times 270\mu m$ 316L stainless steel powder bed layer with 80 μm powder thickness is placed on the top of a flat 316L stainless steel substrate with a thickness of 80 μm.

The fluid dynamics of the melt pool in the laser melting process is mainly driven by Marangoni force and the recoil pressure at the liquid metal surface. As Figure 9 (a) shows, the Marangoni

force acts along the tangential direction of the pool surface [60]. It is driven by the temperature dependency of the surface tension. For metals, the surface tension decreases with increasing temperature. To reduce the surface energy, the higher surface tension fluid at the low-temperature region pulls the fluid from the center of the laser spot. On the other hand, the recoil pressure acts on along the normal direction of the surface, increasing exponentially with respect to temperature (in Figure 9 (b)). It pushes the high-temperature melt pool center downward to form a depression zone as illustrated in the figure. Thus, the surface morphology of the laser melted powder bed is formed by the combination of Marangoni convection and recoil pressure, and the recoil pressure dominates at higher temperatures. Since the magnitude of recoil pressure is an exponential function of temperature (Equation (9)), whereas the Marangoni convection is caused by the linear temperature dependence of the surface tension, a depression zone will form in the laser spot center, where the highest temperature exists.

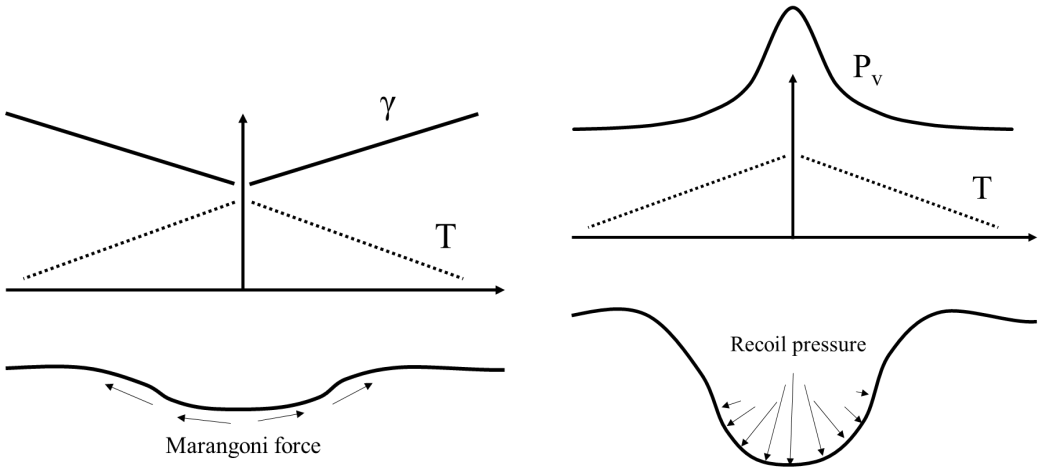

Figure 9: Illustration of (a) the Marangoni effect and (b) the recoil pressure.

The simulation results with different scan speeds from the CFD model are presented in Figure 10. For each of the three cases, the energy density is sufficiently high to vaporize the metal and form a depression zone at the melt pool center, since the vaporized gas at the center region results in localized recoil pressure, which pushes the center of the pool surface downward. Laser heat is mainly absorbed in the laser beam center region. Due to the Marangoni effect, the high-temperature molten metal at the beam center region flows outward to either front or rear of the beam center. For the part of the molten metal that flows towards the rear, heat could be brought away easily in the liquid, so that the temperature near the beam center is reduced. On the other hand, for the part of the molten metal that goes to the front, the flow is suppressed since the nearby material is still solid. The high-temperature liquid is accumulated at the front region of the beam center so that most of the evaporation occurs along the beam centerline and a small region in the front of the laser spot center. This effect is clearly shown in Figure 10(a), where the molten material is pushed from the laser center to the tail region of the melt pool, which increases the thickness of the melt pool tail region, and the melting front shows a higher temperature up to the boiling point. Although the laser power is enough to penetrate the 80 μm powder bed and melt the substrate, there are lack-of-fusion pores observed in the 0.28 m/s scan speed case, as shown in Figure 10 (c).

The thermal gradients and cooling rates at the melt pool tails (labeled in Figure 10(a)) with different scan speeds were analyzed based on Equations 17 and 18. The solidification fronts for three cases are also labeled in the green contour lines in Figure 10. The thermal gradients are normal to the solidification front at those three points, therefore, the thermal gradient directions are in the x-z plane with a small angle with respect to the +x axis (as shown in Figure 10(a)).

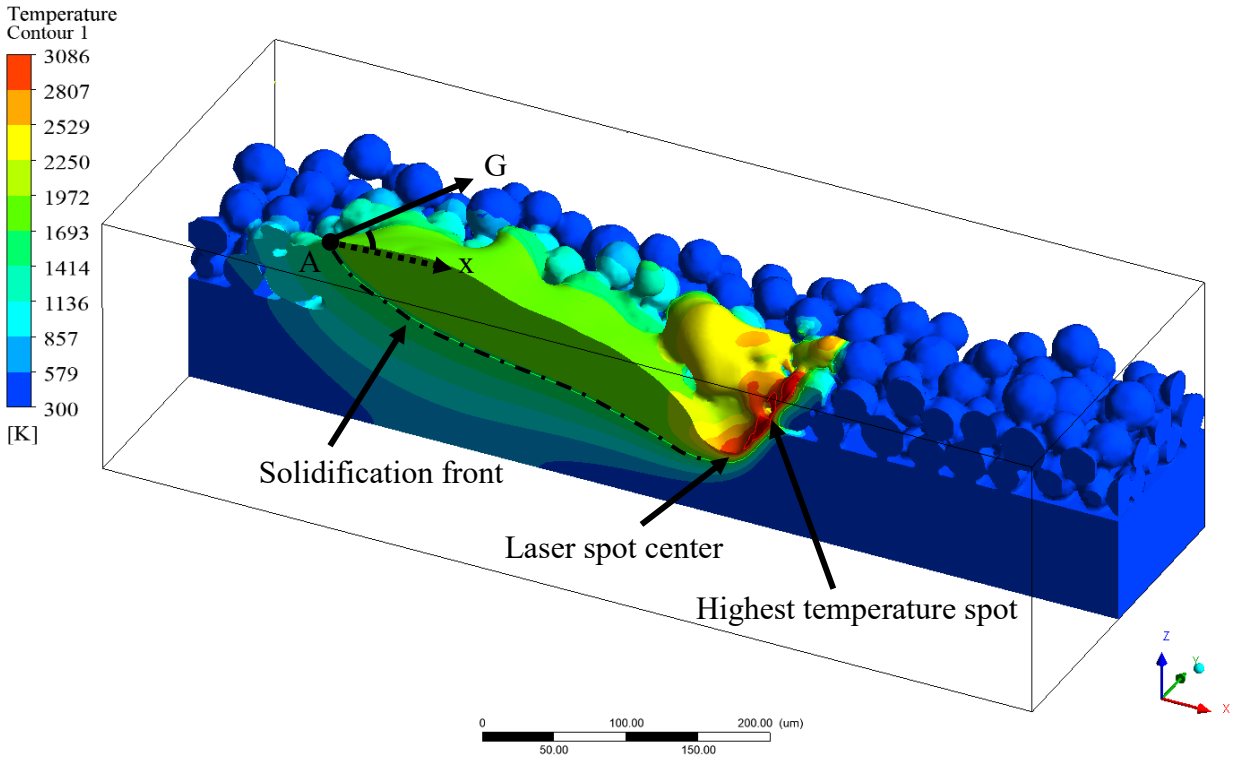
Temperature
Contour 1
3086
2807
2529
2250
1972
1693
1414
1136
857
579
300
[K]
G
A
x
Solidification front
Laser spot center
Highest temperature spot
0
100.00
200.00 (um)
50.00
150.00
Z
Y
X

(a)

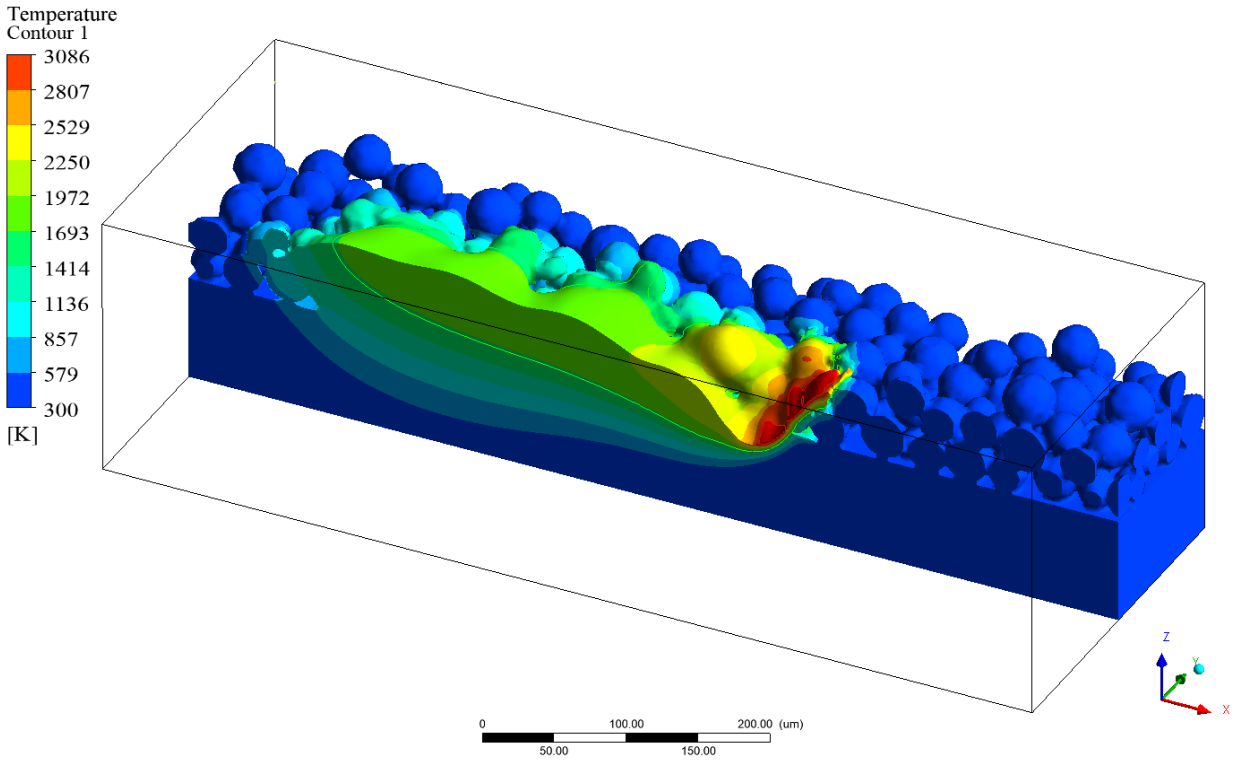
Temperature
Contour 1
3086
2807
2529
2250
1972
1693
1414
1136
857
579
300
[K]
0
100.00
200.00 (um)
50.00
150.00
Z
Y
X

(b)

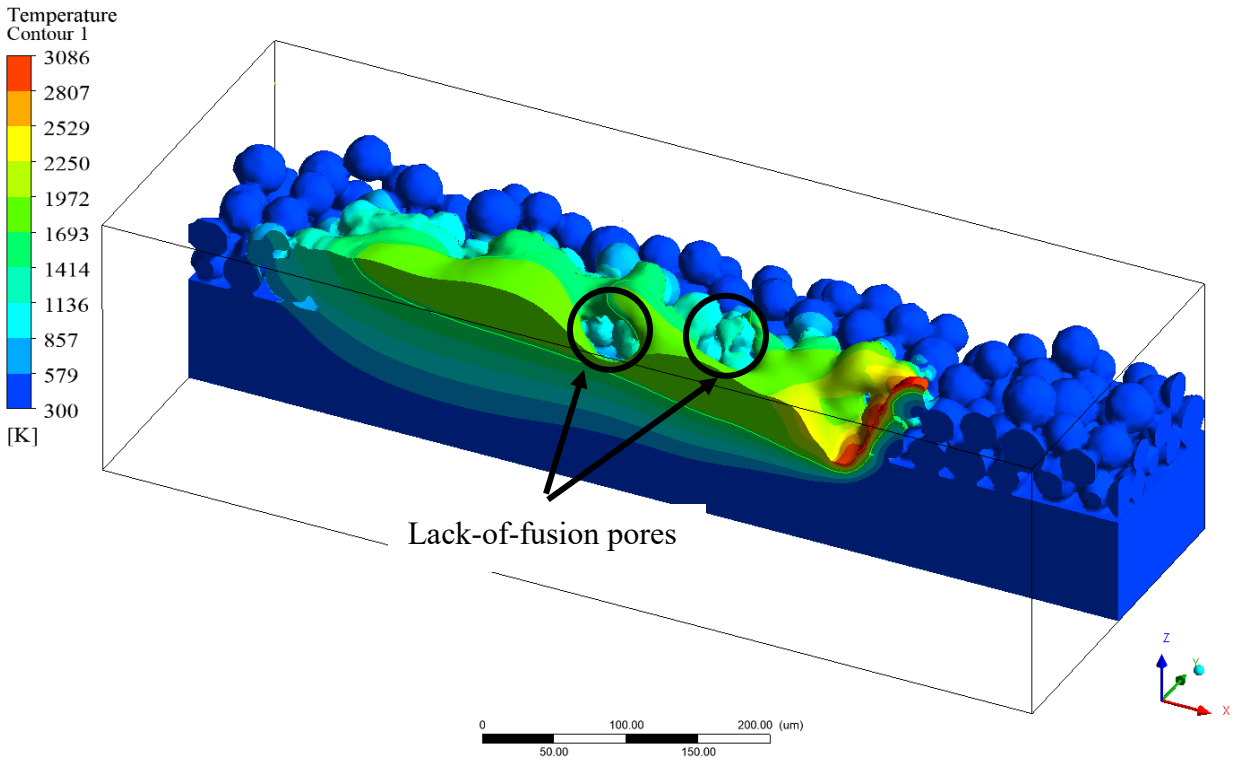
Temperature
Contour 1
3086
2807
2529
2250
1972
1693
1414
1136
857
579
300
[K]
Lack-of-fusion pores
0
100.00
200.00 (um)
50.00
150.00
Z
Y
X

(c)

Figure 10: Melt pool configurations of the powder bed at varying scan speeds (a) 0.12 m/s, (b) 0.20 m/s, (c) 0.28 m/s. Green and red contour lines show the melting and evaporation fronts, respectively.

The melt pool depth results predicted in this work are compared with the experimental work by Yadroitsev *et al*.[41]. The comparison is plotted in Figure 11. At higher scan speeds, the energy density decreases, such that the melt pool depth decreases. The relation between scan speed and melt pool depth is non-linear. Both recoil pressure and Marangoni force contribute to the deepening of the melt pool. The recoil pressure deepens the melt pool by pushing the center region free surface downward so that the material at a deeper region will be melted. On the other hand, due to the temperature dependence of surface tension, the liquid with a higher temperature at the center region will be pushed away to the outside of the melt pool by Marangoni force, therefore more material at the center will be melted, thus deepens the melt pool. The magnitude of recoil pressure is an exponential function of temperature, whereas the Marangoni force is a linear function of temperature. When the energy density is high, recoil pressure increases much faster than Marangoni force. Recoil pressure pushes the molten metal downward to form an even deeper melt pool. However, when the energy density is low, the dominance of recoil pressure decreases, therefore the melt pool depth is shallower. Therefore, although the energy density is linearly increased, the melt pool depth is non-linear, since the portions of contribution from recoil pressure and Marangoni force are different. Although there is about 5 μm difference between modeling and experiment result, the CFD model predicts a decent result in general.

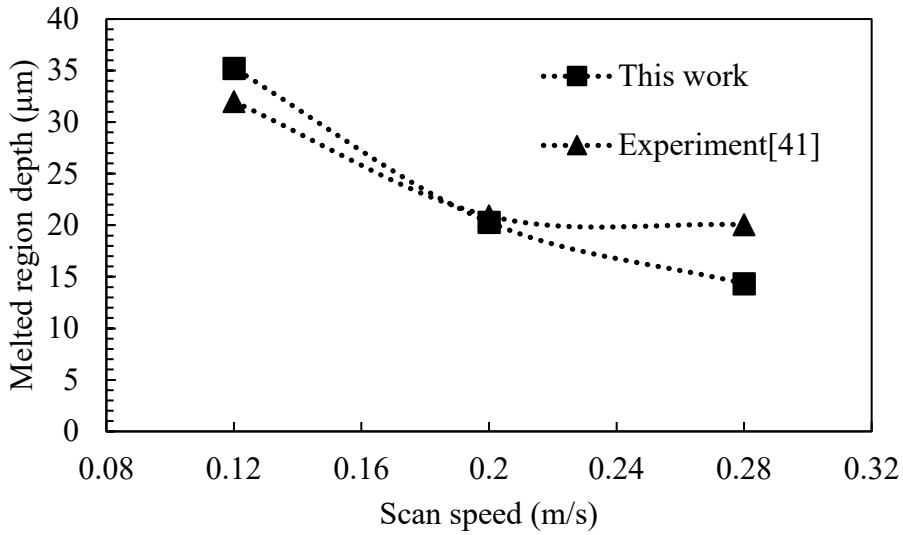

Figure 11: Melt pool depth with scan speed of 0.12, 0.20, 0.28 m/s and comparison with the experiment[41].

Cooling rate and thermal gradient are obtained by the analysis of laser centerline temperature distribution. At the melt pool tail surface, the thermal gradient G (Figure 10 a) around the solidus temperature is calculated based on the following equation [61]:

$$G = \frac{T_1 - T_2}{(d_2 - d_1)} \tag{17}$$

where T_1 (unit: K) is the solidus $T_{solidus}$, $T_2 = T_{solidus} - 100K$. d_1 (unit: m) and d_2 (unit: m) are the locations of T_1 and T_2 on the centerline, respectively. This equation calculates the temperature slope between the locations of d_1 and d_2. The relationship between the cooling rate $\varepsilon(unit: \frac{K}{S})$ and the temperature gradient G is:

$$\varepsilon = RG \tag{18}$$

where the solidification rate R equals to the scan speed V (unit: m/s) at the centerline.

Figure 12 shows the dependency of both the cooling rate and temperature gradient on the laser scan speed. Comparing the three cases with different scan speeds, although the input energy

densities are different, the peak temperatures in the melt pool are similar since the molten metal flows rapidly from the hotter region to the colder region. As a result, the temperature distributions at the solidification front of the melt pool are similar in these three cases, which lead to a similar magnitude of the thermal gradient in the solidification front region, as shown in Figure 12. The slight difference between the three cases could be a result of different localized flow patterns. However, the cooling rates follow an increasing trend with respect to scan speed, since the solidification rate is larger for higher scans. The effect of cooling rate and the thermal gradient will affect the microstructure of the grains, and the details will be explained in the CA modeling results in the next paragraphs.

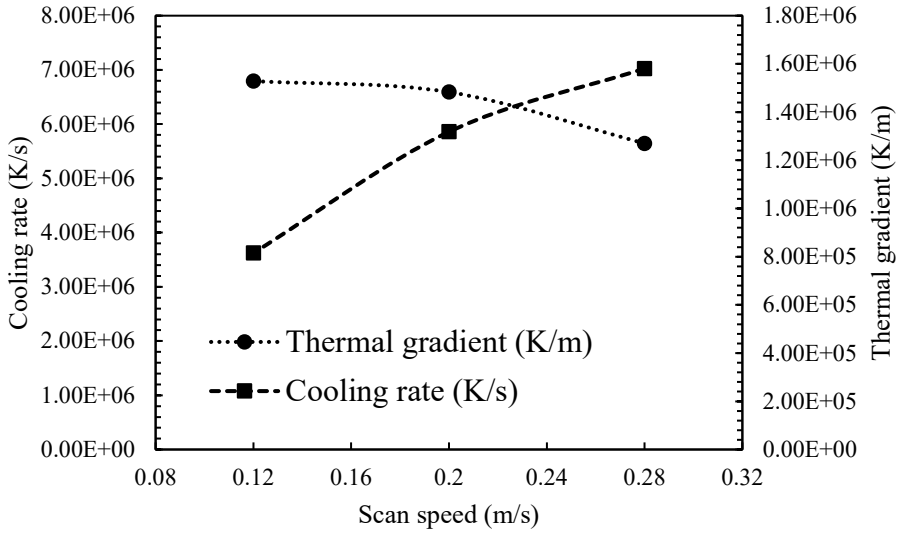

Figure 12: Cooling rate and thermal gradient during solidification at varying scan speeds.

The temperature and volume of fluid results from the CFD modeling are imported to the CA model. A smaller simulation domain is considered in the CA model, as a much finer mesh is required to represent the grain structure. The CFD results are mapped to the CA model by linear interpolation with respect to space and time. The simulation result is shown in Figure 13.

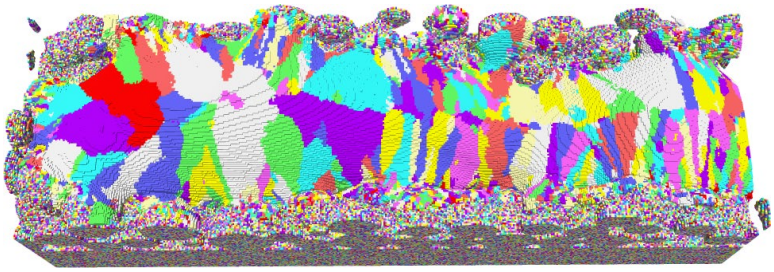

Figure 13: Top view of the CA simulated grain structure of 316L stainless steel powder at scan speeds of 0.12 m/s.

A frame of the CA result during the solidification is shown in Figure 14(a). The gray color shows the liquid metal, white color shows air, and the other colors show the grain orientations in the solid metal. During the solidification process, the grains grow from the bottom of the melt pool with a fast growth rate, whereas the fusion lines at the left and right sides of the melt pool have almost no grain growth. This could be explained by the CFD result in Figure 14(b), which shows the cooling rate at the same location as Figure 14(a). The grain growth rate is proportional to the cooling rate[62], which is the product of thermal gradient G and solidification rate $R = Vcos\theta$, where V is the scan speed, and θ is the angle between the laser scan speed direction and the solidification direction. Thus, $R = V$ at centerline, and $R \approx 0$ at the fusion line at two sides of the melt pool (as shown in Figure 14(c) for illustration). Therefore, in Figure 14(b), the cooling rate has its maximum at the bottom of the centerline region where solidification occurs, and its minimum at the fusion line at left and right sides, which leads to the corresponding grain growth rate distribution in Figure 14(a).

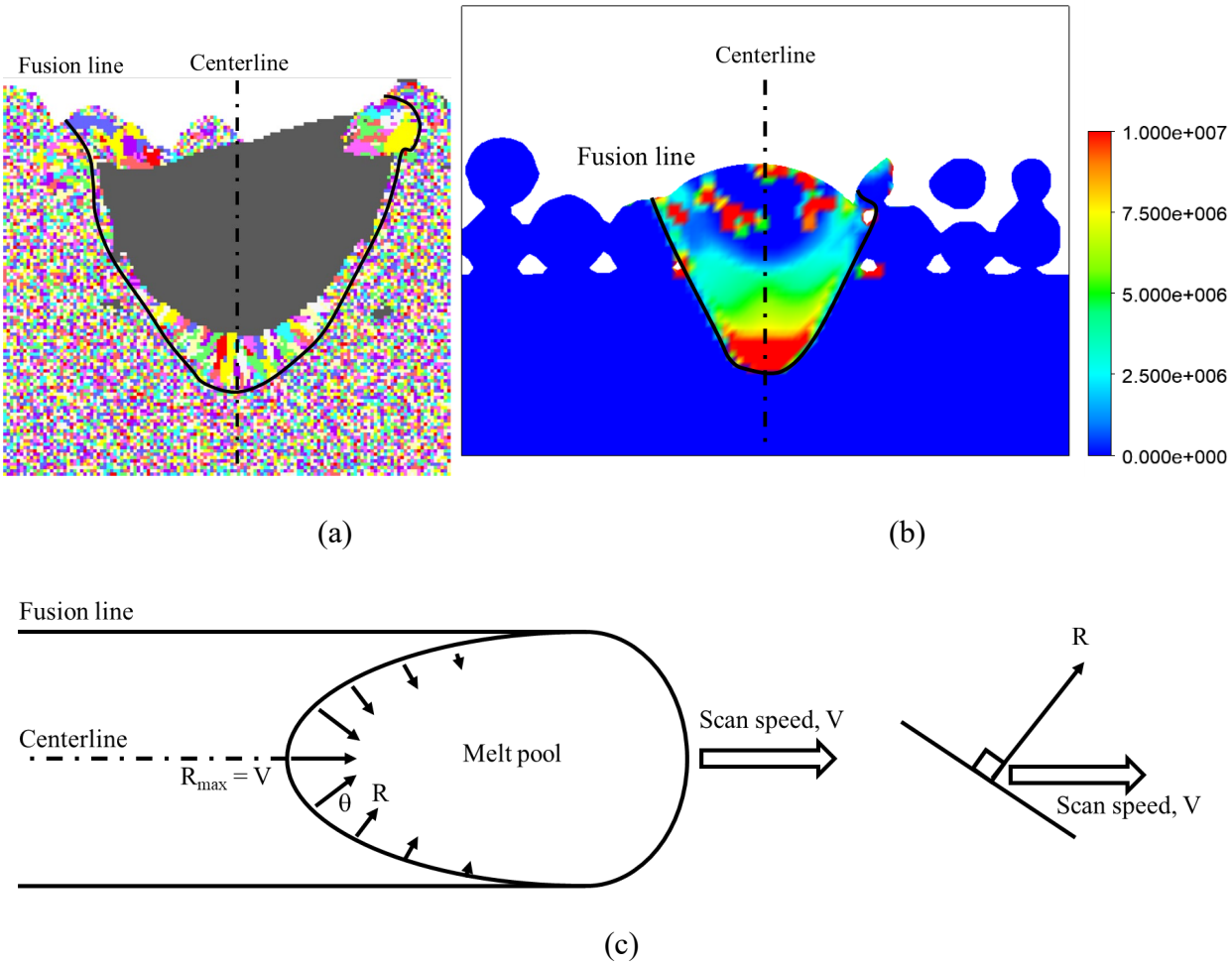

Figure 14: Cross-sectional view of (a) grain configuration during the CA solidification process, (b) the CFD model predicted cooling rate (unit: K/s), and (c) a schematic to illustrate the laser solidification process (top view of the melt pool).

In Figure 15, the simulated cross-section view of the solidified grain structure of 0.12 m/s scan speed is compared with the experimentally measured cross-sectional images from literature[41]. In the experiment result (Figure 15 (a)), the grain structure is a mixed columnar and equiaxed type. Columnar grains grow upward from the melt pool boundary, and large equiaxed grains can be found in the top region near the centerline. There are many factors that can affect the grain size. Substrate grain size may have effect on the boundary grain size of the build layer. If the substrate has a large grain size, then the boundary grains of the build layer would be larger. For

example, Tang *et al.* reported the effect of cooling rate on the cell spacing in AlSi10Mg [63]. In general, for metallic materials, the most commonly used equation that relates grain size and cooling rate is to investigate the dendrite spacing [62]. The dendrite spacing, α, during solidification is related to the cooling rate, ε, is defined by: $\alpha = A\varepsilon^{-n}$, where A and n are constants. Therefore, larger cooling rate will end up to finer grains, which is shown in the modeling result, where the grain size increases as they are far away from the bottom melt pool boundary. In the experiment result, although most of the grain growth is initiated by boundary nucleation at the bottom boundary of the melt pool, there is a small region of equiaxed grains at the top of the melt pool are formed by volume nucleation [22]. This mixed "boundary-volume" nucleated grain structure may be observed in welding and single-track laser scanning experiments [62]. To represent the volume nucleation formed equiaxed grains in the simulation model, an undercooling-nucleation density function is necessary as an input. However, this data is currently not available for the specific material in this study. Therefore, the model in this work cannot capture the equiaxed grains initiated by volume nucleation, which shows a difference at the top region of the melt pool with the experiment. Longitudinal cross-section is also compared with experimental data. The result comparison of laser scan speed of 0.28m/s is shown in Figure 15 (c) and (d). Only columnar grain was observed in the experiment image and the grain width was less than 5 μm. Similar grain structure is observed in the simulation result, where the majority of the grains are columnar parallel to each other, and the grain width is between 2-4μm.

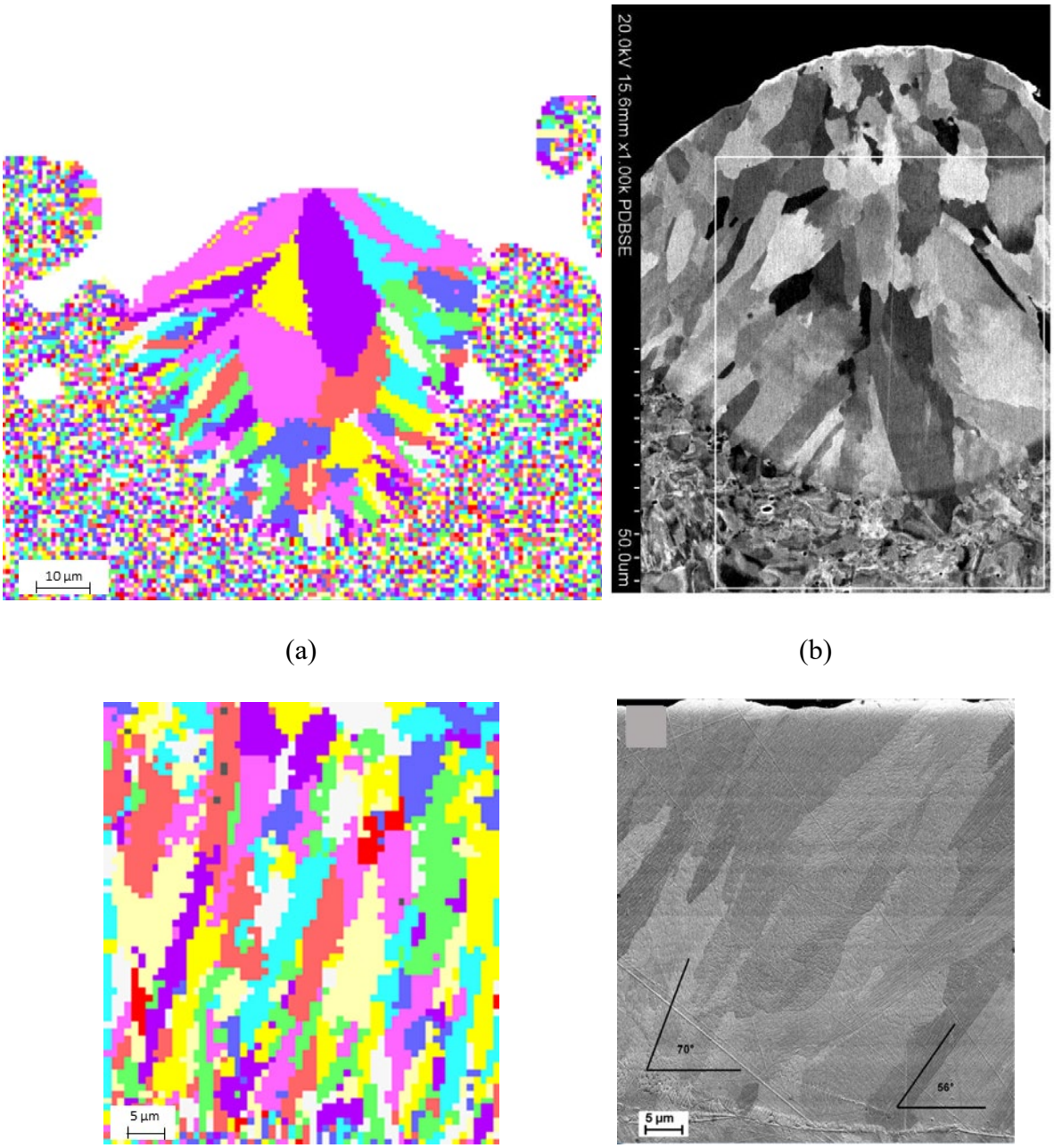

Figure 15: The CA simulated grain structure cross-sectional views: (a) perpendicular to laser moving direction; (c), longitudinal cross-section, and, (b), (d), the corresponding experimentally measured images from Ref.[41].

To study the effects of laser scan speed on the grain structure, the longitudinal cross-section views of CA predicted configuration of the laser melted powder layer with varying scan speeds

are shown in Figure 16(a-c). In all three cases, the cross-section is composed of a large portion of columnar grains with a few equiaxed grains at the centerline. With increasing scan speed, the grain size decreases, due to the larger cooling rate. The angle between grain growth direction and the laser moving direction (horizontally from left to right) is referred to as "laser-grain angle" in the text. In the 0.12 m/s case, the simulation result shows that the laser-grain angle is changing during the growth: at the bottom of the grain, the laser-grain angle is about 70^{o}, where this angle decreases to about 60^{o} at the top surface. As the scan speed increases, this angle difference diminishes. This agrees with the experimental observation by Yadroitsev *et al.*[41]. Depending on the processing conditions, there are two possible grain structure types commonly found in welded metal[62, 64-67]. One type is the "competitive grain growth", where the grains at the fusion line may initially be oriented in a favorable direction for growth, but their direction may become unfavorable as the curved solid/liquid interface changes its position. These grains may then eventually be overgrown by other grains that exhibit more favorable orientation for growth as the solid/liquid interface sweeps through the weld. As a result, the grains at the centerline will grow toward the weld direction. The other type is "centerline grain boundary forming", where the grains grow straight toward the weld centerline until grains growing from each side of the weld intersect, typically leads to a centerline grain boundary. With increasing scan speed, the grain structures transform from "competitive grain growth" type, to "centerline grain boundary forming" type. The laser-grain angle results and their comparisons with experimental data are plotted in Figure 16(d).

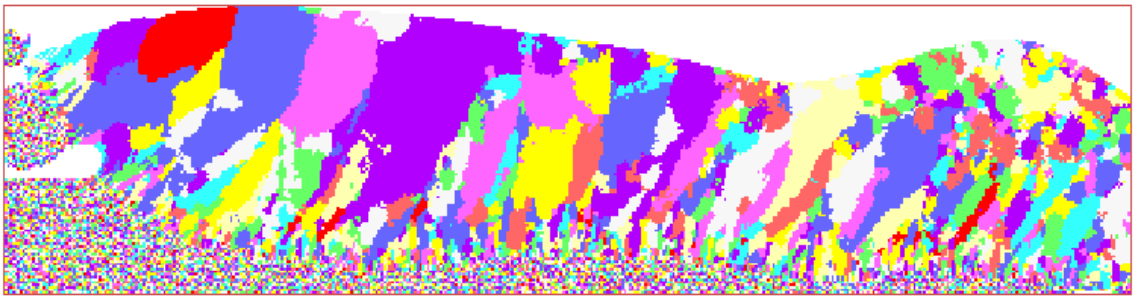

(a)

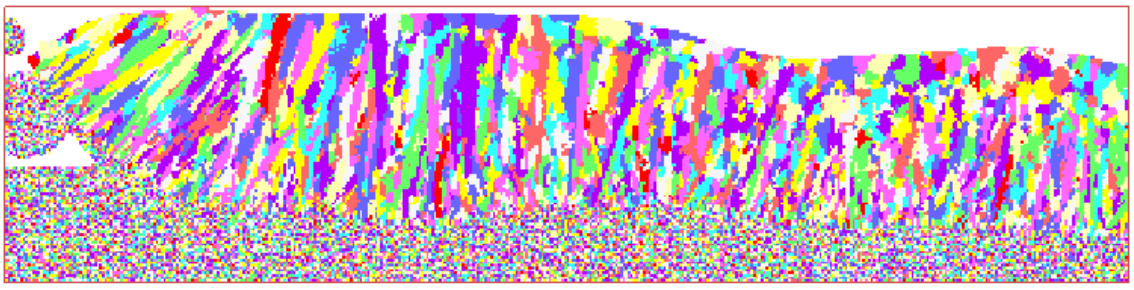

(b)

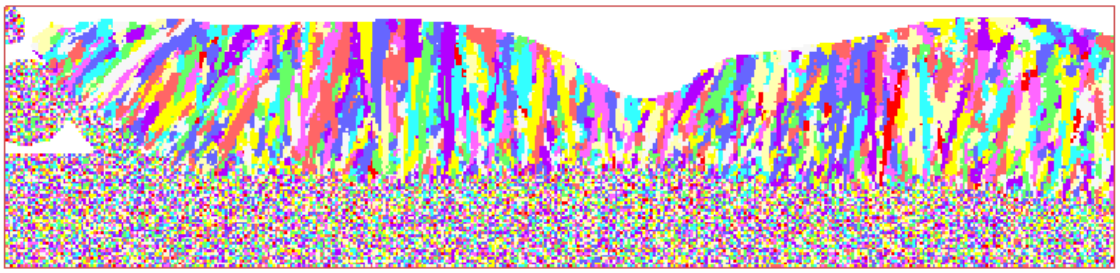

(c)

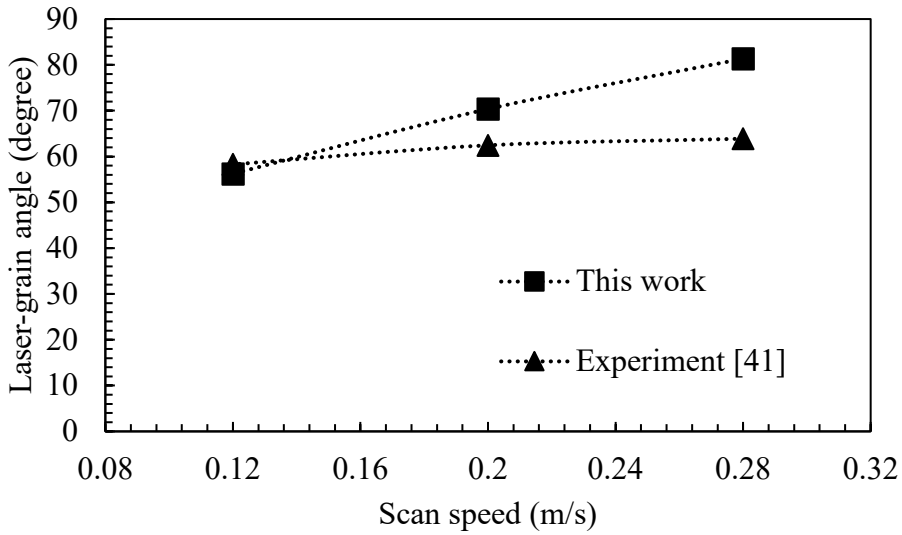

(d)

Figure 16: The longitudinal cross-sectional view of microstructures simulated by CA method, with scan speed of (a) 0.12 m/s, (b) 0.20 m/s, and (c) 0.28 m/s; (d) Simulated laser-grain angles in comparison with experimental data [41].

4. Conclusions

A novel simulation framework is developed, which is capable to simulate the solidification microstructure evolution in randomly packed L-PBF 316 stainless steel power bed. The major conclusions are summarized as follows:

1. The fluid dynamics of the melt pool flow in the laser melting process is mainly driven by the competing Marangoni force and the recoil pressure at the liquid metal surface. The Marangoni force acts along the tangential direction of surface, and the recoil pressure due to evaporation acts along the normal direction of the surface, increasing exponentially with respect to temperature. It pushes the high temperature melt pool center downward to form a depression zone.

2. The effect of recoil pressure goes larger when the energy density increases. The evaporation occurs at the front end of the laser spot, so that the recoil pressure pushes the liquid metal backward to the tail region at the melt pool.
3. Simulated melt pool depths are compared well with the experimental data. Higher scan speeds lead to smaller melt pool depth, and lack-of-fusion pores are formed.
4. An "air-metal" two-phase CA based on the "modified decentered square" method is proposed. The metal free surface change during the solidification process is modeled in the CA. The simulated solidification microstructure using the CA model is in a good agreement with experimental data.
5. The solidification microstructure evolution is investigated using the modeling framework. Higher laser scan speed leads to finer grain size, larger laser-grain angle, and higher columnar grain contents, which are consistent with experimental observations.

Acknowledgments

JZ acknowledges the financial support provided by NSF/CMMI Award (No. 1936290, Program Manager: Dr. Steven Schmid), Walmart Foundation (project title: Optimal Plastic Injection Molding Tooling Design and Production through Advanced Additive Manufacturing), and Praxair's TruForm™ AMbition Grant.

References

[1] Y. Zhang, L. Wu, X. Guo, S. Kane, Y. Deng, Y.-G. Jung*, et al.*, "Additive Manufacturing of Metallic Materials: A Review," *Journal of Materials Engineering and Performance,* vol. 27, pp. 1-13, 2018.

[2] M. Yan and P. Yu, "An Overview of Densification , Microstructure and Mechanical Property of Additively Manufactured Ti-6 Al-4 V — Comparison among Selective Laser Melting , Electron Beam Melting , Laser Metal Deposition and Selective Laser Sintering , and with Conventional Powder Metallurgy," 2017.

[3] S. Bontha, N. W. Klingbeil, P. A. Kobryn, and H. L. Fraser, "Thermal process maps for predicting solidification microstructure in laser fabrication of thin-wall structures," *Journal of Materials Processing Technology,* vol. 178, pp. 135-142, 2006/09/14/ 2006.

[4] A. V. Gusarov, I. Yadroitsev, P. Bertrand, and I. Smurov, "Model of Radiation and Heat Transfer in Laser-Powder Interaction Zone at Selective Laser Melting," *Journal of Heat Transfer,* vol. 131, pp. 072101-072101-10, 2009.

[5] J. Zhou, Y. Zhang, and J. K. Chen, "Numerical Simulation of Random Packing of Spherical Particles for Powder-Based Additive Manufacturing," *Journal of Manufacturing Science and Engineering,* vol. 131, pp. 031004-031004-8, 2009.

[6] T. DebRoy, H. L. Wei, J. S. Zuback, T. Mukherjee, J. W. Elmer, J. O. Milewski*, et al.*, "Additive manufacturing of metallic components – Process, structure and properties," *Progress in Materials Science,* vol. 92, pp. 112-224, 2018/03/01/ 2018.

[7] S. Shrestha and K. Chou, "A build surface study of Powder-Bed Electron Beam Additive Manufacturing by 3D thermo-fluid simulation and white-light interferometry," *International Journal of Machine Tools and Manufacture,* vol. 121, pp. 37-49, 2017/10/01/ 2017.

[8] S. I. Anisimov and V. A. Khokhlov, *Instabilities in Laser-Matter Interaction*: CRC Press, 1995.

[9] Z. Zhang and G. Gogos, "Theory of shock wave propagation during laser ablation," *Physical Review B,* vol. 69, p. 235403, 06/08/ 2004.

[10] S. A. Khairallah and A. Anderson, "Mesoscopic simulation model of selective laser melting of stainless steel powder," *Journal of Materials Processing Technology,* vol. 214, pp. 2627-2636, 2014/11/01/ 2014.

[11] W. Tan and Y. C. Shin, "Multi-scale modeling of solidification and microstructure development in laser keyhole welding process for austenitic stainless steel," *Computational Materials Science,* vol. 98, pp. 446-458, 2015/02/15/ 2015.

[12] C. Zhao, K. Fezzaa, R. W. Cunningham, H. Wen, F. De Carlo, L. Chen*, et al.*, "Real-time monitoring of laser powder bed fusion process using high-speed X-ray imaging and diffraction," *Scientific Reports,* vol. 7, p. 3602, 2017/06/15 2017.

[13] J. Zhang, Y. Zhang, W. H. Lee, L. Wu, H.-H. Choi, and Y.-G. Jung, "A multi-scale multi-physics modeling framework of laser powder bed fusion additive manufacturing process," *Metal Powder Report,* vol. 73, pp. 151-157, 2018/05/01/ 2018.

[14] S. Ly, A. M. Rubenchik, S. A. Khairallah, G. Guss, and M. J. Matthews, "Metal vapor micro-jet controls material redistribution in laser powder bed fusion additive manufacturing," *Scientific Reports,* vol. 7, p. 4085, 2017/06/22 2017.

[15] Y. Zhang and J. Zhang, "Finite Element Simulation and Experimental Validation of Distortion and Cracking Failure Phenomena in Direct Metal Laser Sintering Fabricated Component," *Additive Manufacturing,* vol. 16, pp. 49–57, 2017.
[16] Y. Zhang and J. Zhang, "Sintering phenomena and mechanical strength of nickel based materials in direct metal laser sintering process—a molecular dynamics study," *Journal of Materials Research,* vol. 31, pp. 2233-2243, 2016.
[17] M. Xia, D. Gu, G. Yu, D. Dai, H. Chen, and Q. Shi, "Porosity evolution and its thermodynamic mechanism of randomly packed powder-bed during selective laser melting of Inconel 718 alloy," *International Journal of Machine Tools and Manufacture,* vol. 116, pp. 96-106, 2017/05/01/ 2017.
[18] C. Panwisawas, B. Perumal, R. M. Ward, N. Turner, R. P. Turner, J. W. Brooks*, et al.*, "Keyhole formation and thermal fluid flow-induced porosity during laser fusion welding in titanium alloys: Experimental and modelling," *Acta Materialia,* vol. 126, pp. 251-263, 2017/03/01/ 2017.
[19] S. A. Khairallah, A. T. Anderson, A. Rubenchik, and W. E. King, "Laser powder-bed fusion additive manufacturing: Physics of complex melt flow and formation mechanisms of pores, spatter, and denudation zones," *Acta Materialia,* vol. 108, pp. 36-45, 4/15/ 2016.
[20] T. T. Roehling, S. S. Q. Wu, S. A. Khairallah, J. D. Roehling, S. S. Soezeri, M. F. Crumb*, et al.*, "Modulating laser intensity profile ellipticity for microstructural control during metal additive manufacturing," *Acta Materialia,* vol. 128, pp. 197-206, 2017/04/15/ 2017.
[21] C. A. Gandin and M. Rappaz, "A coupled finite element-cellular automaton model for the prediction of dendritic grain structures in solidification processes," *Acta Metallurgica et Materialia,* vol. 42, pp. 2233-2246, 1994/07/01/ 1994.
[22] C. A. Gandin and M. Rappaz, "A 3D Cellular Automaton algorithm for the prediction of dendritic grain growth," *Acta Materialia,* vol. 45, pp. 2187-2195, 1997/05/01/ 1997.
[23] W. Wang, P. D. Lee, and M. McLean, "A model of solidification microstructures in nickel-based superalloys: predicting primary dendrite spacing selection," *Acta Materialia,* vol. 51, pp. 2971-2987, 2003/06/11/ 2003.
[24] R. C. Atwood, P. D. Lee, R. S. Minisandram, and R. M. F. Jones, "Multiscale modelling of microstructure formation during vacuum arc remelting of titanium 6-4," *Journal of Materials Science,* vol. 39, pp. 7193-7197, 2004/12/01 2004.
[25] W. S. Ping, L. D. Rong, G. J. Jie, L. C. Yun, S. Y. Qing, and F. H. Zhi, "Numerical simulation of microstructure evolution of Ti-6Al-4V alloy in vertical centrifugal casting," *Materials Science and Engineering: A,* vol. 426, pp. 240-249, 2006/06/25/ 2006.
[26] T. Carozzani, H. Digonnet, and A. G. Ch, "3D CAFE modeling of grain structures: application to primary dendritic and secondary eutectic solidification," *Modelling and Simulation in Materials Science and Engineering,* vol. 20, p. 015010, 2012.
[27] S. Chen, G. Guillemot, and C.-A. Gandin, "3D Coupled Cellular Automaton (CA)-Finite Element (FE) Modeling for Solidification Grain Structures in Gas Tungsten Arc Welding (GTAW)," *ISIJ international,* vol. 54, pp. 401-407, 2014 2014.
[28] A. R. A. Dezfoli, W.-S. Hwang, W.-C. Huang, and T.-W. Tsai, "Determination and controlling of grain structure of metals after laser incidence: Theoretical approach," *Scientific Reports,* vol. 7, p. 41527, 01/30/online 2017.

[29] S. Chen, G. Guillemot, and C.-A. Gandin, "Three-dimensional cellular automaton-finite element modeling of solidification grain structures for arc-welding processes," *Acta Materialia,* vol. 115, pp. 448-467, 2016/08/15/ 2016.
[30] W. Tan, N. S. Bailey, and Y. C. Shin, "Numerical Modeling of Transport Phenomena and Dendritic Growth in Laser Spot Conduction Welding of 304 Stainless Steel," *Journal of Manufacturing Science and Engineering,* vol. 134, pp. 041010-041010-8, 2012.
[31] A. Rai, M. Markl, and C. Körner, "A coupled Cellular Automaton–Lattice Boltzmann model for grain structure simulation during additive manufacturing," *Computational Materials Science,* vol. 124, pp. 37-48, 2016/11/01/ 2016.
[32] A. Zinoviev, O. Zinovieva, V. Ploshikhin, V. Romanova, and R. Balokhonov, "Evolution of grain structure during laser additive manufacturing. Simulation by a cellular automata method," *Materials & Design,* vol. 106, pp. 321-329, 2016/09/15/ 2016.
[33] J. Zhang, F. Liou, W. Seufzer, and K. Taminger, "A coupled finite element cellular automaton model to predict thermal history and grain morphology of Ti-6Al-4V during direct metal deposition (DMD)," *Additive Manufacturing,* vol. 11, pp. 32-39, 2016/07/01/ 2016.
[34] C. Panwisawas, C. Qiu, M. J. Anderson, Y. Sovani, R. P. Turner, M. M. Attallah*, et al.*, "Mesoscale modelling of selective laser melting: Thermal fluid dynamics and microstructural evolution," *Computational Materials Science,* vol. 126, pp. 479-490, 2017/01/01/ 2017.
[35] Y. Lian, S. Lin, W. Yan, W. Liu, and G. Wagner, *A parallelized three-dimensional cellular automaton model for grain growth during additive manufacturing*, 2018.
[36] W. Yan, Y. Lian, C. Yu, O. L. Kafka, Z. Liu, W. K. Liu*, et al.*, "An integrated process–structure–property modeling framework for additive manufacturing," *Computer Methods in Applied Mechanics and Engineering,* vol. 339, pp. 184-204, 2018/09/01/ 2018.
[37] C. Kloss, C. Goniva, A. Hager, S. Amberger, and S. Pirker, "Models, algorithms and validation for opensource DEM and CFD–DEM," *Progress in Computational Fluid Dynamics, an International Journal,* vol. 12, pp. 140-152, 2012.
[38] W.-H. Lee, Y. Zhang, and J. Zhang, "Discrete element modeling of powder flow and laser heating in direct metal laser sintering process," *Powder Technology,* vol. 315, pp. 300–308, 2017.
[39] C. Kloss, C. Goniva, A. Hager, S. Amberger, and S. J. P. i. C. F. D. Pirker, an International Journal, "Models, algorithms and validation for opensource DEM and CFD–DEM," vol. 12, pp. 140-152, 2012.
[40] L. E. Silbert, D. Ertaş, G. S. Grest, T. C. Halsey, D. Levine, and S. J. Plimpton, "Granular flow down an inclined plane: Bagnold scaling and rheology," *Physical Review E,* vol. 64, p. 051302, 10/25/ 2001.
[41] I. Yadroitsev, P. Krakhmalev, I. Yadroitsava, S. Johansson, and I. Smurov, "Energy Input Effect on Morphology and Microstructure of Selective Laser Melting Single Track from Metallic Powder," *Journal of Materials Processing Technology,* vol. 213, pp. 606-613, 2013 2013.
[42] G. Yablokova, M. Speirs, J. Van Humbeeck, J. P. Kruth, J. Schrooten, R. Cloots*, et al.*, "Rheological behavior of β-Ti and NiTi powders produced by atomization for SLM production of open porous orthopedic implants," *Powder Technology,* vol. 283, pp. 199-209, 2015/10/01/ 2015.

[43] W. E. King, A. T. Anderson, R. M. Ferencz, N. E. Hodge, C. Kamath, S. A. Khairallah*, et al.*, "Laser powder bed fusion additive manufacturing of metals; physics, computational, and materials challenges," *Applied Physics Reviews,* vol. 2, p. 041304, 2015/12/01 2015.
[44] "ANSYS Fluent release 17.0," 2016.
[45] C. Mickael, C. Muriel, M. Philippe Le, G. Sadok, and B. Mikhaël, "A new approach to compute multi-reflections of laser beam in a keyhole for heat transfer and fluid flow modelling in laser welding," *Journal of Physics D: Applied Physics,* vol. 46, p. 505305, 2013.
[46] S. Pang, W. Chen, and W. Wang, "A Quantitative Model of Keyhole Instability Induced Porosity in Laser Welding of Titanium Alloy," *Metallurgical and Materials Transactions A,* vol. 45, pp. 2808-2818, 2014/06/01 2014.
[47] C. S. Wu, H. T. Zhang, and J. Chen, "Numerical simulation of keyhole behaviors and fluid dynamics in laser–gas metal arc hybrid welding of ferrite stainless steel plates," *Journal of Manufacturing Processes,* vol. 25, pp. 235-245, 2017/01/01/ 2017.
[48] C. Jung-Ho and N. Suck-Joo, "Implementation of real-time multiple reflection and Fresnel absorption of laser beam in keyhole," *Journal of Physics D: Applied Physics,* vol. 39, p. 5372, 2006.
[49] D. B. Kothe, L. A. N. Laboratory, R. C. Mjolsness, U. S. D. o. Defense, M. D. Torrey, U. S. N. Aeronautics*, et al.*, *RIPPLE: A Computer Program for Incompressible Flows with Free Surfaces*: Available to DOE and DOE contractors from OSTI, 1991.
[50] J. Zhou and H.-L. Tsai, "Porosity Formation and Prevention in Pulsed Laser Welding," *Journal of Heat Transfer,* vol. 129, pp. 1014-1024, 2006.
[51] J. Wang, M. Wang, and Z. Li, "A lattice Boltzmann algorithm for fluid–solid conjugate heat transfer☆☆The present work was supported by the National Natural Science Foundation of China (Grant No. 59995550-2)," *International Journal of Thermal Sciences,* vol. 46, pp. 228-234, 2007/03/01/ 2007.
[52] J. J. Valencia and P. N. Quested, "Thermophysical properties," in *Casting, ASM Handbook*. vol. 15, ed: ASM International, 2008, pp. 468-481.
[53] M. Rappaz and C.-A. Gandin, "Probabilistic modelling of microstructure formation in solidification processes," *J Acta metallurgica et materialia,* vol. 41, pp. 345-360, 1993.
[54] I. Yadroitsev, P. Krakhmalev, I. Yadroitsava, P. Bertrand, and I. Smurov, "Energy input effect on the microstructure, Energy input effect on the microstructure, morphology and stability of single track from morphology and stability of single track from metallic powder in selective laser melting," 2012.
[55] W. Kurz, B. Giovanola, and R. Trivedi, "Theory of microstructural development during rapid solidification," *Acta Metallurgica,* vol. 34, pp. 823-830, 1986/05/01/ 1986.
[56] S. Chen, "Three dimensional Cellular Automaton – Finite Element (CAFE) modeling for the grain structures development in Gas Tungsten / Metal Arc Welding processes," Ecole Nationale Supérieure des Mines de Paris, 2014.
[57] "Mathworks MATLAB," 2018.
[58] A. Stukowski, "Visualization and analysis of atomistic simulation data with OVITO–the Open Visualization Tool," *Modelling and Simulation in Materials Science and Engineering,* vol. 18, p. 015012, 2009/12/15 2009.

[59] Y. Lian, S. Lin, W. Yan, W. K. Liu, and G. J. J. C. M. Wagner, "A parallelized three-dimensional cellular automaton model for grain growth during additive manufacturing," vol. 61, pp. 543-558, 2018.
[60] J.-M. Drezet, S. Pellerin, C. Bezençon, and S. Mokadem, "Modelling Marangoni convection in laser heat treatment," *J. Phys. IV France,* vol. 120, pp. 299-306, 2004 2004.
[61] J. C. Heigel, "Solid Freeform Fabrication," *Proceedings of the 28th Annual International,* pp. 1340-1348, 2017.
[62] J. N. DuPont, "Fundamentals of Weld Solidification," *ASM Handbook,* vol. 6A, pp. 96-113, 2011.
[63] M. Tang, P. C. Pistorius, S. Narra, and J. L. Beuth, "Rapid Solidification: Selective Laser Melting of AlSi10Mg," *JOM,* vol. 68, pp. 960-966, March 01 2016.
[64] L. Wu and J. Zhang, "Phase Field Simulation of Dendritic Solidification of Ti-6Al-4V During Additive Manufacturing Process," *JOM,* vol. 70, pp. 2392-2399, October 01 2018.
[65] J. Zhang, L. Wu, Y. Zhang, and L. Meng, "Phase field simulation of dendritic microstructure in additively manufactured titanium alloy," *Metal Powder Report,* vol. 74, pp. 20-24, 2019/01/01/ 2019.
[66] Y. Zhang, X. Xiao, and J. Zhang, "Kinetic Monte Carlo simulation of sintering behavior of additively manufactured stainless steel powder particles using reconstructed microstructures from synchrotron X-ray microtomography," *Results in Physics,* vol. 13, p. 102336, 2019/06/01/ 2019.
[67] J. Zhang and Y.-G. Jung, "Additive Manufacturing: Materials, Processes, Quantifications and Applications," ed: Elsevier, 2018.